Applied Energy 277 (2020) 115555

Contents lists available at ScienceDirect

Applied Energy

journal homepage: www.elsevier.com/locate/apenergy

Modeling of the effects of cathode catalyst layer design parameters on performance of polymer electrolyte membrane fuel cell

Pu He[a], Yu-Tong Mu[b], Jae Wan Park[c], Wen-Quan Tao[a,*]

[a] Key Laboratory of Thermo-Fluid Science and Engineering of MOE, School of Energy and Power Engineering, Xi'an Jiaotong University, Xi'an, Shaanxi 710049, China
[b] School of Human Settlements and Civil Engineering, Xi'an Jiaotong University, Shaanxi 710049, China
[c] Department of Mechanical and Aerospace Engineering, University of California, One Shields Ave., Davis, CA 95618, USA

HIGHLIGHTS

- An improved three-dimensional multiphase non-isothermal PEMFC model is established.
- The effects of five design parameters of CCL on cell performance are investigated.
- Low Pt loading is more likely to cause oxygen starvation.
- Increase of I/C ratio is better for the uniformity of membrane water distribution.

ARTICLE INFO

Keywords:
Polymer electrolyte membrane fuel cell
Three-dimensional multiphase non-isothermal model
Cathode catalyst layer
Pt loading
Pt/C ratio
I/C ratio

ABSTRACT

A comprehensive macroscopic three-dimensional multiphase non-isothermal polymer electrolyte membrane fuel cell (PEMFC) model coupled with an improved electrochemical kinetics model considering the geometric structure parameters of the cathode catalyst layer (CCL) and oxygen transport process in CCL is developed. The effects of five CCL design parameters are investigated. It is found that the Pt loading of CCL has a significant effect on the performance, a low platinum (Pt) loading is more likely to cause oxygen starvation. The increase of Pt/C ratio can promote the performance significantly at a lower Pt/C ratio. A lower I/C ratio is good for the enhancement of limiting current density, a larger I/C ratio is good for the increase of maximum power density, and the increase in I/C ratio is better for the uniformity of membrane water distribution. With the decrease of carbon particle radius, the oxygen concentration on the Pt surface of CCL increases significantly. The increase of electrochemical specific area (ECSA) of Pt particles can promote the performance. In addition, a discussion on applicability of new correlations of capillary pressure-water saturation and effective diffusivity and their effects on the predicted PEMFC performance is presented.

1. Introduction

Polymer electrolyte membrane fuel cell (PEMFC) has attracted more and more attention in the past years due to its outstanding merits such as high energy efficiency, low pollution, and low operating temperature, thus, it has been recognized as one of the most promising energy conversion devices in the 21th century. However, the commercialization of PEMFC is still greatly challenged by the expensive cost. Among many factors affecting the cost of PEMFC, the Pt loading in the catalyst layer is an important one. According to the hydrogen and fuel cells program review from DOE [1], the platinum (Pt) loading should be reduced to 0.125 mg cm^{-2} at least before 2020, and it should be further reduced to 0.088 mg cm^{-2}. But for the current, the average Pt loading is around 0.25 mg cm^{-2}. Thus, it is of great challenge to reduce the Pt loading without a sacrifice of performance to meet the demand of commercialization.

The catalyst layer (CL) is composed of carbon particles, Pt particles, ionomer, and pores. The electrochemical reaction occurs at the interfaces of Pt particle/carbon particle/ionomer, and the microstructure of CL has an important effect on the performance [2-5]. In order to optimize the design of CL and make a further decrease of the Pt loading, the characteristics of the transport processes of gas, water, electrons, and proton in CL should be revealed deeply. Due to the complex microstructure of CL, the direct measurement of the heat and mass transfer in CL is still very difficult [6-9]. Mathematical modeling and numerical simulation provide another useful way to investigate the multiphase

* Corresponding author.
E-mail address: wqtao@mail.xjtu.edu.cn (W.-Q. Tao).

https://doi.org/10.1016/j.apenergy.2020.115555
Received 11 April 2020; Received in revised form 7 July 2020; Accepted 17 July 2020
Available online 31 July 2020
0306-2619/

Nomenclature

A	cell geometric area (m^2)
a_{ECSA}	electrochemical specific area (m^2_{Pt} g^{-1}_{Pt})
a_{Pt}	active volumetric surface area of platinum
c_p	specific heat capacity (J mol^{-1} K^{-1})
c_i	gas species molar concentration (mol m^{-3})
$c^{ref}_{H_2}$	reference concentration of hydrogen (mol m^{-3})
$c^{ref}_{O_2}$	reference concentration of oxygen (mol m^{-3})
$c^{Pt}_{O_2}$	oxygen concentration on the Platinum surface (mol m^{-3})
D	diffusion coefficient (m^2 s^{-1})
$ECSA$	electrochemical specific area (m^2_{Pt} g^{-1}_{Pt})
E_r	thermodynamic reversible cell voltage (V)
EW	equivalent weight of membrane (kg mol^{-1})
F	Faraday's constant (96,487C mol^{-1})
h	condensation latent heat (J mol^{-1})
$H_{O_2,ion}$	Henry's constant of oxygen in the ionomer (Pa mol^{-1} m^{-3})
I	ionic current density (A m^{-2})
I/C	ionomer to carbon weight ratio
j	reaction rate (A m^{-3})
$j^{ref}_{0,a}$	volumetric reference exchange current density in anode (A m^{-3})
$j^{ref}_{0,c}$	volumetric reference exchange current density in cathode (A m^{-3})
K	intrinsic permeability
k	liquid phase relative permeability
k^{eff}	effective thermal conductivity (W m^{-1} K^{-1})
$\dot{m}$	mass flux (kg m^{-2} s^{-1})
m_{Pt}	platinum loading (mg cm^{-2})
M	molecular weight (g mol^{-1})
n_d	electro-osmotic drag coefficient
p	pressure (Pa)
Pt/C	platinum to carbon weight ratio
r_{pore}	pore diameter of GDL/MPL/CL (m)
r_C	carbon particle radius (m)
r_{Pt}	platinum particle radius (m)
R	universal gas constant (J mol^{-1} K^{-1})
R_{CCL}	transport resistance of CCL (s m^{-1})
RH	relative humidity
$R^{Pt}_{O_2}$	local transport resistance of oxygen (s m^{-1})
$R_{ion,int}$	interfacial transport resistance of ionomer (s m^{-1})
R^{eff}_{ion}	effective diffusion resistance (s m^{-1})
$R^{eff}_{Pt,int}$	effective interfacial transport resistance of platinum (s m^{-1})
S	source term (kg m^{-3} s^{-1}, mol m^{-3} s^{-1}, W m^{-3}), entropy (J mol^{-1} K^{-1})
s_{lq}	liquid saturation
t	time (s)
T	temperature (K)
$\vec{u}$	velocity (m s^{-1})
U_{PtO}	equilibrium potential (V)
V_{out}	output voltage (V)
$wt\%$	platinum weight percentage of the Pt/C catalyst
x	total catalyst particle number fraction
y_{bare}	weight fraction of the bare carbon

Greek letters

α	transfer coefficient
β	reaction order for oxygen reduction reaction
δ	thickness (m)
ε	porosity
ε_C	volume fraction of carbon particle
ε_{ion}	volume fraction of ionomer
ε_{Pt}	volume fraction of Platinum particle
ϕ	potential (V)
γ	water phase change rate (s^{-1})
η	overpotential (V)
κ	conductivity (S m^{-1})
λ	membrane water content in ionomer
μ	dynamic viscosity (kg m^{-1} s^{-1})
θ	contact angle
θ_{PtO}	Pt-oxide coverage
ρ	density (kg m^{-3})
σ	surface tension coefficient (N m^{-1})
ω	energy parameter for the Temkin isotherm
ξ	stoichiometry ratio

Subscripts and superscripts

0	intrinsic value
a	anode
ACL	anode catalyst layer
act	activation
BP	bipolar plate
c	cathode
CCL	cathode catalyst layer
CH	channel
CL	catalyst layer
E	energy
eff	effective
ele	electronic
eq	equilibrium
g	gas phase
GDL	gas diffusion layer
i	the ith component
ion	ionic/ionomer
Kn	Knudsen
lq	liquid water
m	mass
MEM	membrane
mole	molecular
MPL	microporous layer
mw	membrane water
Pt	platinum
ref	reference
sat	saturation
u	momentum
v-l	vapor to liquid (vice versa)
v-m	vapor to membrane water (vice versa)

transport phenomenon and electrochemical reaction in the CL especially for the optimization of CL design parameters. Recently, a comprehensive review was made for the transport and performance model in PEMFC in [2], where it is indicated that to simulate the catalyst layer accurately is a challenge since its structure characteristics and properties cover the extent from microscopic to macroscopic scales. In a very recent study conducted by Mu et al. [10], a comprehensive mesoscopic analyses considering the coupled oxygen and water transport processes in a complicated CL microstructure have been performed. They suggested that both the reduced oxygen permeation coefficient in ionomer thin-film and the adsorption resistance at Pt surface account for the local transport resistance.

In order to characterize the transport process in CL, a lot of CL models have been developed. Earlier CL models treated CL as a

boundary condition [3,4], and later it is treated as a thin layer of homogeneous porous material with multi-components including the ionomer, void pores and carbon skeleton [5-9]. In these models, the amount of Pt particles and complex CL structures are not considered, thus these models often underestimated the effects of fuel gas transport resistance especially under high current density, leading to some inaccuracy in the prediction of performance. In order to further consider the effects of the structure of CL on the mass transfer process and the fuel cell performance, various agglomerate models are proposed, which consider the co-existence of Pt particles, carbon particles, ionomer, and gas pores, and consider the transport resistance of fuel gas. These models can more quantitatively reveal the influence of the structure parameters of CL such as the Pt loading, agglomerate size, ionomer thickness and species transport process in CL on the performance. However, Due to the limitation of experimental methods and the multi-scale complexity of the CL structure, even now the real structure of agglomerates is not clear enough, and controversies still exist on the agglomerate. For example, some authors assume that the agglomerate is filled with ionomer [11-14], while others consider that it is filled with water [15,16]. For the agglomerate and ionomer sizes previous studies [17-20] assumed that agglomerates vary from 100 nm to 2000 nm, and the thickness of the ionomer ranges from 10 nm to 100 nm. However, such large variations of agglomerate size and ionomer thickness have not been observed by the microscopy techniques [21,22]. Moreover, in the studies of Litster [23,24] and Greszler [25], it is found that the agglomerate size can rarely exceed 300 nm. Therefore, the agglomerate model still needs further improvements to get more verification from experimental results.

From view point of practical application, the homogeneous model of CL is very convenient for engineering design. If some advantages of the agglomerate models, say Pt loading, interfacial resistances [25-28], etc., can be somehow adopted into the homogenous model, that will greatly improves model accuracy while still keeps its advantage of simplicity. Such an improvement has been made in [29]. In the study of [29], Hao et al. developed a novel comprehensive electrode model to consider the effect of interfacial resistance of ionomer, diffusion resistance of ionomer and interfacial resitance of Pt particle during the oxygen transport in CL. This model takes into account the composition of electrode paticles and implants the results into the homogeheous electrode model. This improvement is very helpful for the engineering simulations and design of PEMFC. However, the PEMFC model tested in the study of Hao et al. [29] is actually a single phase model in that the water in flow channels is assumed to be vapor. A test of a more complicated PEMFC model and study on the effects of various electrode composition factors on the performance are highly required.

In this study, a macroscopic three-dimensional multiphase non-isothermal PEMFC model with 13 governing equations is developed and an improved cathode electrochemical kinetics model is adopted maily based on [29]. The effects of CCL design parameters such as Pt loading, Pt/C ratio, I/C ratio, carbon particle radius and electrochemical specific area (ECSA) of Pt particles on the oxygen transport resistance in CCL, performance, water transport, oxygen transport process are investigated. In the following, the numerical model is first described in Section 2. Then in Section 3 results of the simulation on the effects of Pt loading, Pt/C ratio, I/C ratio, carbon particle radius and electrochemical specific area of Pt particles in CCL are discussed in detail. Finally, some conclusions are drawn in Section 4.

2. Numerical model

2.1. Computational domain

A three-dimensional domain including the bipolar plates (BPs), flow channels, gas diffusion layers (GDLs), microporous layers (MPLs), CLs and membrane is shown in Fig. 1. In order to save computational time, a half cell with symmetrical boundary condition is utilized. The related physical/geometrical parameters and operating conditions are listed in Table 1.

2.2. Conservation equations

The present model is governed by 13 conservation equations, including the conservation of mass and momentum of gas mixture, gas species, liquid pressure, liquid saturation, membrane water, energy, electronic potential, and ionic potential. In the following the 13 governing equations are presented with their solution regions indicated clearly in the brakets.

Mass of gas mixture (solved in flow channels, GDLs, MPLs, CLs):

$$\frac{\partial}{\partial t}(\varepsilon(1-s_{\mathrm{lq}})\rho_{\mathrm{g}}) + \nabla\cdot(\rho_{\mathrm{g}}\vec{u}_{\mathrm{g}}) = S_{\mathrm{m}} \tag{1}$$

Momentum of gas mixture (solved in flow channels, GDLs, MPLs, CLs):

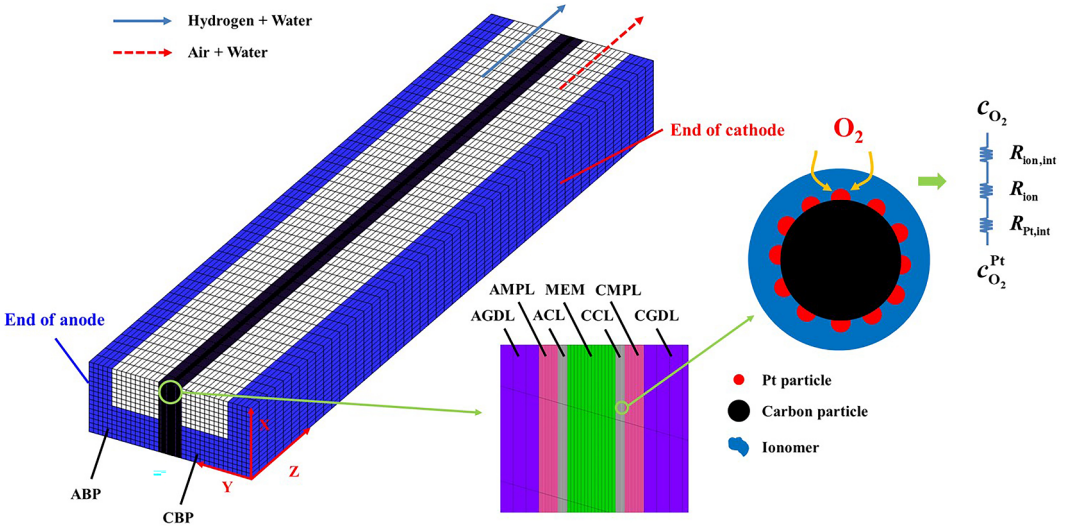

Fig. 1. Computational domain and mesh.

Table 1
Cell properties and operating conditions.

Parameters	Value	Source Refs
Channel length; width; height	50; 0.8; 1.0 mm	
Land width	0.7 mm	
BP height	1.5 mm	
Thicknesses of GDL; MPL; CL; MEM	0.19; 0.02; 0.01; 0.0508 mm	[63]
Density of MEM	1980.0 kg m^{-3}	[8]
Equivalent weight of MEM	1.1 kg mol^{-1}	[8]
Porosities of GDL; MPL; CL	$\varepsilon_{GDL,MPL,CL}$ = 0.6; 0.4; 0.3	
Intrinsic permeabilities of GDL; MPL; CL; MEM	$K^0_{GDL,MPL,CL,MEM}$ = 2×10^{-12}; 1×10^{-12}; 1×10^{-13}; 2×10^{-20} m^2	[49-51]
Specific heat capacities of GDL; MPL; CL; MEM; BP	$(c_p)_{GDL,MPL,CL,MEM,BP}$ = 568; 3300; 3300; 833; 1580 J kg^{-1} K^{-1}	[8,49]
Thermal conductivities of GDL; MPL; CL; MEM; BP	$k_{GDL,MPL,CL,MEM,BP}$ = 1.0; 1.0; 1.0; 0.95; 20 W m^{-1} K^{-1}	[8,49]
Electrical conductivities of GDL; MPL; CL; BP	$\kappa_{GDL,MPL,CL,BP}$ = 7000; 2000; 2000; 20,000 S m^{-1}	[49]
Contact angles of GDL; MPL; CL	θ_{GDL} = 120°; θ_{MPL} = 115°; θ_{CL} = 100°	[52,53]
Contact angles at GDL/channel interface; BP/channel interface	$\theta_{GDL/channel}$ = 120°; $\theta_{BP/channel}$ = 90°	[54]
Stoichiometry ratio of anode; cathode for 1.0 A cm^{-2} current density	$\xi_{a,c}$ = 3.0; 3.0	[63]
Relative humidity of inlet gas	$RH_{a,c}$ = 1.0	[63]
Operating temperature	T_0 = 353.15 K	[63]

Table 2
Transport parameters.

Parameters	Correlation/value	Unit	Source Refs
Liquid water dynamic viscosity, T (K)	$\mu_{lq} = 2.414\times10^{-5}\times10^{247.8/(T-140.0)}$	kg m^{-1} s^{-1}	[8]
Gas mixture dynamic viscosity	$\mu_g = \sum_i \frac{X_i\mu_i}{\sum_j X_j\phi_{ij}}$	kg m^{-1} s^{-1}	[8]
Gas diffusivity (i: H_2, O_2, vapor)	$D_i = \left(\frac{1}{D_{Kn,i}} + \frac{1}{D^{a,c}_{mole,i}}\right)^{-1}$	m^2 s^{-1}	[65]
Molecular diffusivity of hydrogen in anode, T (K), p (Pa)	$D^a_{mole,H_2} = 1.055\times10^{-4}\left(\frac{T}{333.15}\right)^{1.5}\left(\frac{101,325}{p}\right)$	m^2 s^{-1}	[8]
Molecular diffusivity of oxygen in cathode, T (K), p (Pa)	$D^c_{mole,O_2} = 2.652\times10^{-5}\left(\frac{T}{333.15}\right)^{1.5}\left(\frac{101,325}{p}\right)$	m^2 s^{-1}	[8]
Molecular diffusivity of vapor in anode, T (K), p (Pa)	$D^a_{mole,H_2O} = 1.055\times10^{-4}\left(\frac{T}{333.15}\right)^{1.5}\left(\frac{101,325}{p}\right)$	m^2 s^{-1}	[8]
Molecular diffusivity of vapor in cathode, T (K), p (Pa)	$D^c_{mole,H_2O} = 2.982\times10^{-5}\left(\frac{T}{333.15}\right)^{1.5}\left(\frac{101,325}{p}\right)$	m^2 s^{-1}	[8]
Knudsen diffusivity of hydrogen, T (K)	$D_{Kn,H_2} = \frac{d_{GDL/MPL/CL}}{3}\left(\frac{8RT}{\pi M_{H_2}}\right)^{0.5}$	m^2 s^{-1}	[55]
Knudsen diffusivity of oxygen, T (K)	$D_{Kn,O_2} = \frac{d_{GDL/MPL/CL}}{3}\left(\frac{8RT}{\pi M_{O_2}}\right)^{0.5}$	m^2 s^{-1}	[55]
Knudsen diffusivity of vapor, T (K)	$D_{Kn,H_2O} = \frac{d_{GDL/MPL/CL}}{3}\left(\frac{8RT}{\pi M_{H_2O}}\right)^{0.5}$	m^2 s^{-1}	[55]
Oxygen diffusivity in ionomer, T (K)	$D_{O_2,ion} = 1.0\times10^{-10}(0.1543(T-273)-1.65)$	m^2 s^{-1}	[56]
Henry's constant of oxygen at ionomer surface	$H_{O_2,ion} = \frac{101325}{4.408 - 0.09712\lambda}$	Pa mol^{-1} m^{-3}	[21]
Typical pore diameter of CL; MPL; GDL	$d_{GDL/MPL/CL}$ = 10×10^{-6}; 300×10^{-9}; 100×10^{-9}	m	[57,58,65]
Liquid water density	ρ_{lq} = 970.0	kg m^{-3}	
Evaporation, condensation rates	$\gamma_{v\text{-}l,\,l\text{-}v}$ = 100	s^{-1}	[15]
Membrane water and water vapor phase change rate	$\gamma_{v\text{-}d}$ = 1.3	s^{-1}	[30]
Entropy change of reaction in anode	ΔS_a = 130.68	J mol^{-1} K^{-1}	[59]
Entropy change of reaction in cathode	ΔS_c = 32.55	J mol^{-1} K^{-1}	[59]
Condensation latent heat	h = 44900.0	J mol^{-1}	[59]
Electro-osmotic drag coefficient	$n_d = \frac{2.5\lambda}{22}$		[60]
Membrane water diffusivity	$D_{mw} = \begin{cases} 3.1\times10^{-7}\lambda(\exp(0.28\lambda)-1.0)\exp(-2346/T) & 0<\lambda<3 \\ 4.17\times10^{-8}\lambda(161\exp(-\lambda)+1)\exp(-2346/T) & 3\leqslant\lambda<17 \\ 4.1\times10^{-10}(\lambda/25)^{0.15}(1+\tanh((\lambda-2.5)/1.4)) & \lambda\geqslant17 \end{cases}$	m^2 s^{-1}	[61]
Ionic conductivity	$\kappa_{ion} = (0.5139\lambda - 0.326)\exp(1268(1/303.15 - 1/T))$	S m^{-1}	[60]
Equilibrium membrane water content	$\lambda_{eq} = \begin{cases} 0.043 + 17.81a - 39.85a^2 + 36.0a^3 & 0\leqslant a\leqslant1 \\ 14.0 + 1.4(a-1.0) & 1<a\leqslant3 \end{cases}$		[60]
Water activity	$a = 2s_{lq} + c_{H_2O}RT/p_{sat}$		[8]
Saturation pressure	$\log_{10}(p_{sat}/101325) = -2.1794 + 0.02953(T-273.15) - 9.1837\times10^{-5}(T-273.15)^2 + 1.4454\times10^{-7}(T-273.15)^3$	Pa	[60]
Bruggeman correction	$D_i^{eff} = D_i\varepsilon^{1.5}$		

$$\frac{\partial}{\partial t}\left(\frac{\rho_g \vec{u}_g}{\varepsilon(1-s_{lq})}\right)+\nabla\cdot\left(\frac{\rho_g \vec{u}_g \vec{u}_g}{\varepsilon^2(1-s_{lq})^2}\right)=-\nabla p_g+\mu_g\nabla\cdot\left(\nabla\left(\frac{\vec{u}_g}{\varepsilon(1-s_{lq})}\right)+\left(\frac{\vec{u}_g^{T}}{\varepsilon(1-s_{lq})}\right)\right)-\frac{2}{3}\mu_g\nabla\left(\nabla\cdot\left(\frac{\vec{u}_g}{\varepsilon(1-s_{lq})}\right)\right)+S_u \tag{2}$$

Gas species (i: H_2, O_2, H_2O. Solved in flow channels, GDLs, MPLs, CLs):

$$\frac{\partial}{\partial t}(\varepsilon(1-s_{lq})\rho_g Y_i)+\nabla\cdot(\rho_g \vec{u}_g Y_i)=\nabla\cdot(\rho_g D_i^{eff}\nabla Y_i)+S_i \tag{3}$$

Liquid pressure (solved in GDLs, MPLs, CLs):

$$\frac{\partial}{\partial t}(\rho_{lq}\varepsilon s_{lq})=\nabla\cdot\left(\rho_l\frac{Kk_{lq}}{\mu_{lq}}\nabla p_{lq}\right)+S_{lq} \tag{4}$$

Liquid water saturation (solved in flow channels):

$$\frac{\partial}{\partial t}(\rho_{lq}s_{lq})+\nabla\cdot(\rho_{lq}\vec{u}_{lq}s_{lq})=0 \tag{5}$$

In this model, the liquid pressure (Eq. (4)) is solved in porous media (GDLs, MPLs, CLs), and the liquid water saturation in the three regions can be obtained by the following Leverett-J function [30]

$$p_c=p_g-p_{lq}=\sigma\cos\theta\left(\frac{\varepsilon}{K}\right)^{0.5}J(s_{lq}) \tag{6}$$

$$J(s_{lq})=\begin{cases}1.42(1-s_{lq})-2.12(1-s_{lq})^2+1.26(1-s_{lq})^3 & \theta<90^o\\ 1.42s_{lq}-2.12s_{lq}^2+1.26s_{lq}^3 & \theta>90^o\end{cases} \tag{7}$$

where σ (N m^{-1}) is the surface tension coefficient, θ is the contact angle of GDL/MPL/CL, ε is the porosity of GDL/ MPL/CL, K (m^2) is the permeability of GDL/MPL/CL. During the transport of liquid water, the liquid pressure is continuous between different porous layers (GDL/ MPL, MPL/CL), but due to the different contact angle, permeability and porosity of the porous layer, the liquid saturation between different porous layer are discontinuous.

Membrane water content (solved in membrane, CLs):

$$\frac{\rho_{MEM}}{EW}\frac{\partial}{\partial t}(\varepsilon_{ion}\lambda)+\nabla\cdot\left(\frac{n_d}{F}\vec{I}_{ion}\right)=\frac{\rho_{MEM}}{EW}\nabla\cdot(D_{mw}^{eff}\nabla\lambda)+S_{mw} \tag{8}$$

Electronic potential (solved in BPs, GDLs, MPLs, CLs):

$$0=\nabla\cdot(\kappa_{ele}^{eff}\nabla\phi_{ele})+S_{ele} \tag{9}$$

Ionic potential (solved in membrane, CLs):

$$0=\nabla\cdot(\kappa_{ion}^{eff}\nabla\phi_{ion})+S_{ion} \tag{10}$$

Energy (solved in the entire domains):

$$\frac{\partial}{\partial t}(\varepsilon s_{lq}c_{p,lq}T+\varepsilon(1-s_{lq})\rho_g c_{p,g}T)+\nabla\cdot(\varepsilon s_{lq}c_{p,lq}\vec{u}_{lq}T+\varepsilon(1-s_{lq})\rho_g c_{p,g}\vec{u}_g T)=\nabla\cdot(k^{eff}\nabla T)+S_E \tag{11}$$

The meanings and units of all the parameters involved in the above equations can be found in the nomenclature.

The reference values of the parameters are listed in Table 1 and

Table 3
Source terms.

Source term		Unit
$S_m=\begin{cases}-S_{v\text{-}l}+S_{v\text{-}m}\cdot\frac{j_a}{2F}M_{H_2} & \text{Anode CL}\\ -S_{v\text{-}l}+S_{v\text{-}m}\cdot\frac{j_c}{4F}M_{O_2} & \text{Cathode CL}\\ -S_{v\text{-}l} & \text{GDLs, MPLs, Channels}\end{cases}$		kg m^{-3} s^{-1}
$S_u=-\frac{\mu_g}{Kk_g}\vec{u}_g$	GDLs, MPLs, CLs	kg m^{-2} s^{-2}
$S_{H_2}=-\frac{j_a}{2F}M_{H_2}$	Anode CL	kg m^{-3} s^{-1}
$S_{O_2}=-\frac{j_c}{4F}M_{O_2}$	Cathode CL	kg m^{-3} s^{-1}
$S_{H_2O}=\begin{cases}-S_{v\text{-}l}+S_{v\text{-}m} & \text{CLs}\\ -S_{v\text{-}l} & \text{GDLs, MPLs, Channels}\end{cases}$		kg m^{-3} s^{-1}
$S_{lq}=\begin{cases}S_{v\text{-}l} & \text{Anode CL, MPLs, GDLs}\\ \frac{j_c}{2F}M_{H_2O}+S_{v\text{-}l} & \text{Cathode CL}\end{cases}$		kg m^{-3} s^{-1}
$S_{mw}=\begin{cases}-\frac{S_{v\text{-}m}}{M_{H_2O}}-\rho_{lq}\frac{K_{MEM}}{M_{H_2O}\mu_{lq}}\frac{p_{lq}^{ACL}-p_{lq}^{CCL}}{\delta_{MEM}\delta_{ACL}} & \text{Anode CL}\\ -\frac{S_{v\text{-}m}}{M_{H_2O}}+\rho_{lq}\frac{K_{MEM}}{M_{H_2O}\mu_{lq}}\frac{p_{lq}^{ACL}-p_{lq}^{CCL}}{\delta_{MEM}\delta_{CCL}} & \text{Cathode CL}\end{cases}$		mol m^{-3} s^{-1}
$S_{ele}=\begin{cases}-j_a & \text{Anode CL}\\ j_c & \text{Cathode CL}\end{cases}$		A m^{-3}
$S_{ion}=\begin{cases}j_a & \text{Anode CL}\\ -j_c & \text{Cathode CL}\end{cases}$		A m^{-3}
$S_E=\begin{cases}\frac{j_a T\Delta S_a}{2F}+j_a\lvert\eta_{act}\rvert+\lVert\nabla\phi_{ele}\rVert^2\kappa_{ele}^{eff}+\lVert\nabla\phi_{ion}\rVert^2\kappa_{ion}^{eff}+h\frac{(S_{v\text{-}l}-S_{v\text{-}m})}{M_{H_2O}} & \text{Anode CL}\\ \frac{j_c T\Delta S_c}{4F}+j_c\lvert\eta_{act}\rvert+\lVert\nabla\phi_{ele}\rVert^2\kappa_{ele}^{eff}+\lVert\nabla\phi_{ion}\rVert^2\kappa_{ion}^{eff}+h\frac{(S_{v\text{-}l}-S_{v\text{-}m})}{M_{H_2O}} & \text{Cathode CL}\\ \lVert\nabla\phi_{ele}\rVert^2\kappa_{ele}^{eff}+h\frac{S_{v\text{-}l}}{M_{H_2O}} & \text{GDLs, MPLs}\\ \lVert\nabla\phi_{ele}\rVert^2\kappa_{ele}^{eff} & \text{BPs}\\ \lVert\nabla\phi_{ion}\rVert^2\kappa_{ion}^{eff} & \text{MEM}\\ 0 & \text{Other zones}\end{cases}$		W m^{-3}
$S_{v\text{-}l}=\begin{cases}\gamma_{v\text{-}l}\varepsilon(1-s_{lq})(c_{H_2O}-c_{sat})M_{H_2O} & c_{H_2O}>c_{sat}\\ \gamma_{l\text{-}v}\varepsilon s_{lq}(c_{H_2O}-c_{sat})M_{H_2O} & c_{H_2O}<c_{sat}\end{cases}$		kg m^{-3} s^{-1}
$S_{v\text{-}m}=\gamma_{v\text{-}m}\frac{\rho_{MEM}}{EW}(\lambda-\lambda_{eq})M_{H_2O}$		kg m^{-3} s^{-1}

Table 2, and the related source terms of the conservation equations are listed in Table 3.The effective diffusion coefficient is determined as follows.

Due to the effect of small pores, the transport of gas species can be affected by the Knudsen diffusion especially in the CL, thus, in this model, an effective diffusivity of gas species in the porous layers is introduced and obtained by

$$D_{\mathrm{i}}^{\mathrm{eff}} = \frac{1}{1/D_{\mathrm{Kn,\,i}} + 1/D_{\mathrm{mole,\,i}}^{\mathrm{a,c}}}\varepsilon^{1.5}(1 - s_{\mathrm{lq}})^{1.5} \tag{12}$$

in which $D_{\mathrm{mole,i}}^{\mathrm{a,c}}$ ($\mathrm{m^2\ s^{-1}}$) and $D_{\mathrm{Kn,i}}$ ($\mathrm{m^2\ s^{-1}}$) are the molecular diffusivity and Knudsen diffusivity, and i = 1,2,3 is for hydrogen, oxygen and water vapor respectively (listed in Table 2), ε is the porosity of GDL/MPL/CL (listed in Table 1).

2.3. Boundary conditions

The mass flow rates at the inlets of anode and cathode are defined as follows,

$$\dot{m}_{\mathrm{a}} = \frac{\rho_{\mathrm{g}}^{\mathrm{a}}\xi_{\mathrm{a}}I_{\mathrm{ref}}A}{2Fc_{\mathrm{H_2}}} \tag{13}$$

$$\dot{m}_{\mathrm{c}} = \frac{\rho_{\mathrm{g}}^{\mathrm{c}}\xi_{\mathrm{c}}I_{\mathrm{ref}}A}{4Fc_{\mathrm{O_2}}} \tag{14}$$

in which $\rho_{\mathrm{g}}^{\mathrm{a}}$ and $\rho_{\mathrm{g}}^{\mathrm{c}}$ ($\mathrm{kg\ m^{-3}}$) are the densities of gas mixture in anode and cathode respectively, ξ_{a} and ξ_{c} are the stoichiometry ratios of anode and cathode respectively, I_{ref} ($\mathrm{A\ cm^{-2}}$) is the reference current density; A ($\mathrm{m^2}$) is the active reaction area of CL, $c_{\mathrm{H_2}}$ and $c_{\mathrm{O_2}}$ ($\mathrm{mol\ m^{-3}}$) are the molar concentration of hydrogen and oxygen in anode and cathode respectively.

The molar concentration of hydrogen and oxygen at the inlets of anode and cathode are determined by

$$c_{\mathrm{H_2}} = \frac{(p_{\mathrm{g}}^{\mathrm{a}} - RH_{\mathrm{a}}p_{\mathrm{sat}})}{RT} \tag{15}$$

$$c_{\mathrm{O_2}} = \frac{0.21(p_{\mathrm{g}}^{\mathrm{c}} - RH_{\mathrm{c}}p_{\mathrm{sat}})}{RT} \tag{16}$$

where $p_{\mathrm{g}}^{\mathrm{a}}$ and $p_{\mathrm{g}}^{\mathrm{c}}$ (Pa) are the inlet pressure at anode and cathode respectively; RH_{a} and RH_{c} are the relative humidity of anode and cathode inlets respectively; p_{sat} (Pa) is the saturation pressure.

In this study, the liquid water saturation conservation equation (Eq. (5)), is solved in the anode and cathode channel, and in order to meet the conservation of liquid water on the interface between channel and GDL, the liquid pressure boundary condition is used on the interface between channel and GDL to solve the liquid pressure equation (Eq. (4)) in GDL. The boundary liquid pressure is calculated by [31]

$$p_{\mathrm{lq}}^{\mathrm{GDL}} = p_{\mathrm{g}}^{\mathrm{GDL}} - p_{\mathrm{c}}^{\mathrm{GDL}} \tag{17}$$

$$p_{\mathrm{c}}^{\mathrm{GDL}} = \sigma\cos\theta_{\mathrm{GDL}}(\varepsilon_{\mathrm{GDL}}/K_{\mathrm{GDL}})^{0.5}J(s_{\mathrm{lq}}^{\mathrm{CH}}) \tag{18}$$

in which the $s_{\mathrm{lq}}^{\mathrm{CH}}$ is obtained by Eq. (5).

On the other hand, the mass flux boundary condition is used on the interface of channel and GDL to solve the liquid water saturation equation (Eq. (5)) in the channel, which is expressed as [31]

$$Flux_{\mathrm{lq}}^{\mathrm{CH}} = -\rho_{\mathrm{lq}}K_{\mathrm{GDL}}k_{\mathrm{lq}}/\mu_{\mathrm{lq}}\nabla p_{\mathrm{lq}}^{\mathrm{GDL}} \tag{19}$$

where $p_{\mathrm{lq}}^{\mathrm{GDL}}$ is the liquid pressure on the GDL side solved by Eq. (4).

The temperatures of the surrounding walls of cell and inlets in the domain are set as the operating temperature.

The electronic potentials at the ends of the BP surfaces for anode and cathode (see Fig. 1) are defined as

$$\phi_{\mathrm{ele}}^{\mathrm{a}} = 0 \tag{20}$$

$$\phi_{\mathrm{ele}}^{\mathrm{c}} = V_{\mathrm{out}} \tag{21}$$

where V_{out} is the output voltage.

The corresponding overpotentials in anode and cathode can be respectively expressed by the following relationships

$$\eta_{\mathrm{act}}^{\mathrm{a}} = \phi_{\mathrm{ele}} - \phi_{\mathrm{ion}} \tag{22}$$

$$\eta_{\mathrm{act}}^{\mathrm{c}} = \phi_{\mathrm{ele}} - \phi_{\mathrm{ion}} - E_{\mathrm{r}} \tag{23}$$

in which the thermodynamic reversible cell voltage E_{r} can be calculated as follows [8],

$$E_{\mathrm{r}} = 1.229 - 0.9\times10^{-3}(T_0 - 298) + \frac{RT_0}{2F}\left(\ln p_{\mathrm{H_2}}^{\mathrm{in}} + \frac{1}{2}p_{\mathrm{O_2}}^{\mathrm{in}}\right) \tag{24}$$

where the inlet patial pressure of hydrogen ($p_{\mathrm{H_2}}^{\mathrm{in}}$, atm) and oxygen ($p_{\mathrm{O_2}}^{\mathrm{in}}$, atm), operating temperature (volume averaged temperature, K) are used.

No-slip boundary condition is employed for all velocities on the solid walls, and if not specially described, zero flux boundary condition is applied on all external boundaries for the transport scalars in Eqs. (1–5) and Eqs. (8–10).

2.4. Determination of anode/cathode electrical current

The reaction rate of anode (j_{a}, $\mathrm{A\ m^{-3}}$) is calculated by the following Butler-Volmer equation

$$j_{\mathrm{a}} = (1 - s_{\mathrm{lq}})j_{0,\mathrm{a}}^{\mathrm{ref}}\left(\frac{(1 - s_{\mathrm{lq}})\varepsilon_{\mathrm{ACL}}c_{\mathrm{H_2}}}{c_{\mathrm{H_2}}^{\mathrm{ref}}}\right)^{0.5}\left(\exp\left(\frac{2F\alpha_{\mathrm{a}}}{RT}\eta_{\mathrm{act}}^{\mathrm{a}}\right) - \exp\left(-\frac{2F\alpha_{\mathrm{c}}}{RT}\eta_{\mathrm{act}}^{\mathrm{a}}\right)\right) \tag{25}$$

where $j_{0,\mathrm{a}}^{\mathrm{ref}}$ ($\mathrm{A\ m^{-3}}$) is the volumetric reference exchange current density in anode, $c_{\mathrm{H_2}}^{\mathrm{ref}}$ ($\mathrm{mol\ m^{-3}}$) is the reference concentration of hydrogen, $c_{\mathrm{H_2}}$ ($\mathrm{mol\ m^{-3}}$) is the predicted concentration of hydrogen in anode, $\eta_{\mathrm{act}}^{\mathrm{a}}$ (V) is the predicted activation overpotential of anode, and α is the transfer coefficient.

The above reaction rate equation of the anode is of conventional form of Bulter-Volmer type. To reflect the effects of design parameters of the cathode catalyst layer on the electrochemical reaction rate of CCL, such parammeters should be included in the reaction rate equation. It is the reaction rate equation for the cathode where the effects of these parametrs can be contained. As shown in Fig. 1, the structure of CL includes the carbon particles, Pt particles, ionomer and pores. The oxygen in the pore of the CL dissolves into the ionomer firstly, then it diffuses through the ionomer film, and lastly the oxygen arrives on the surface of Pt particle/carbon particle/ionomer and takes part in the electrochemical reaction. During the transfer process of oxygen, there exist three transport resistances, the interfacial resistance due to the oxygen dissolution in ionomer from pore, diffusion resistance due to the oxygen transfer through the ionomer film, and interfacial resistance on the surface between Pt and ionomer due to the Pt particle and ionomer structure. The reaction rate equation of cathode should take such resistances into considerations. It is here the improved homogeneous catalyst model adopted in this paper deffers from conventional ones.

According to [29], the electrochemical reaction rate of the cathode ($\mathrm{A\ m^{-3}}$) can be calculated as

$$j_{\mathrm{c}} = k_{\mathrm{c}}(c_{\mathrm{o_2}}^{\mathrm{Pt}})^{\beta} \tag{26}$$

where $c_{\mathrm{O_2}}^{\mathrm{Pt}}$ is the oxygen concentration on the Pt surface and β is the reaction order for oxygen reduction reaction, which is fixed as 1.0 in this study.

The coefficient k_{c} can be calculated as [29]

$$k_{\mathrm{c}} = \frac{j_{0,\mathrm{c}}^{\mathrm{ref}}a_{\mathrm{Pt}}(1 - \theta_{\mathrm{PtO}})(1 - s_{\mathrm{lq}})}{4F(c_{\mathrm{o_2}}^{\mathrm{ref}})^{\gamma}}\exp\left(-\frac{\alpha_{\mathrm{c}}F\omega\theta_{\mathrm{PtO}}\eta_{\mathrm{act}}^{\mathrm{c}}}{RT}\right) \tag{27}$$

in which $j_{0,c}^{ref}$ (A m^{-2}) is the surface reference exchange current density in cathode, $c_{O_2}^{ref}$ (mol m^{-3}) is the reference concentration of oxygen, η_{act}^{c} (V) is the activation overpotential of cathode, ω is the energy parameter for the Temkin isotherm [32], θ_{PtO} is the Pt-oxide coverage and a_{Pt} is the active volumetric surface area of Pt.

The parameters a_{Pt}, θ_{PtO} and $c_{O_2}^{Pt}$ can be calculated as follows [29,33].

$$a_{Pt} = \frac{a_{ECSA} m_{Pt}}{\delta_{CCL}} \tag{28}$$

where a_{ECSA} (m_{Pt}^2 g_{Pt}^{-1}) is the ECSA of Pt particles, δ_{CCL} (m) is the thickness of CCL, and m_{Pt} (mg cm^{-2}) is the Pt loading.

The Pt-oxide coverage θ_{PtO} [33], and oxygen concentration on the Pt surface $c_{O_2}^{Pt}$ [29] can be calculated respectively as

$$\theta_{PtO} = \frac{\exp(\alpha_1 F(\eta_{act}^{c} + E_r - U_{PtO})/RT)}{\exp(\alpha_1 F(\eta_{act}^{c} + E_r - U_{PtO})/RT) + \exp(-\alpha_2 F(\eta_{act}^{c} + E_r - U_{PtO})/RT)} \tag{29}$$

$$c_{O_2}^{Pt} = \frac{RT}{H_{O_2,ion}} \frac{c_{O_2}}{(1 + k_c (R_{ion,int} + R_{ion}^{eff} + R_{Pt,int}^{eff})/4Fa_C x)} \tag{30}$$

in which α_1 and α_2 are the transfer coefficients, c_{O_2} (mol m^{-3}) is the oxygen concentration in the pore of CCL, $H_{O_2,ion}$ (Pa mol^{-1} m^{-3}) is Henry's constant of oxygen in the ionomer, U_{PtO} (V) is the equilibrium potential and is fixed as 0.76 V [14], and E_r is the thermodynamic reversible cell voltage calculated by Eq. (24).

The interfacial transport resistance of ionomer $R_{ion,int}$, effective diffusion resistance $R_{ion,int}^{eff}$, and effective interfacial transport resistance of Pt $R_{Pt,int}^{eff}$ can be respectively expressed as below [29], and their detailed derivation can be found in the supplementary material.

$$R_{ion,int} = k_1 \frac{\delta_{ion}}{D_{O_2,ion}} \tag{31}$$

$$R_{ion}^{eff} = \frac{\delta_{ion}}{D_{O_2,ion}} \frac{x\rho_{Pt} r_{Pt} (r_C + \delta_{ion})^2 (1 - wt\%)}{\rho_C r_C^3 wt\% (1 - \theta_{PtO})} \tag{32}$$

$$R_{Pt,int}^{eff} = k_2 \frac{\delta_{ion}}{D_{O_2,ion}} \frac{x\rho_{Pt} r_{Pt} (r_C + \delta_{ion})^2 (1 - wt\%)}{\rho_C r_C^3 wt\% (1 - \theta_{PtO})} \tag{33}$$

where k_1 and k_2 are the interfacial resistance coefficients at the ionomer film surface (see Table 4) and Pt particle surface respectively, δ_{ion} is the ionomer thickness (m), and $D_{O_2,ion}$ (m^2 s^{-1}) is the oxygen diffusivity in the ionomer.

The total catalyst particle number fraction x can be calculated as [29]

$$x = \frac{(1 - wt\%)(1 - y_{bare})}{1 - wt\%(1 - y_{bare})} \tag{34}$$

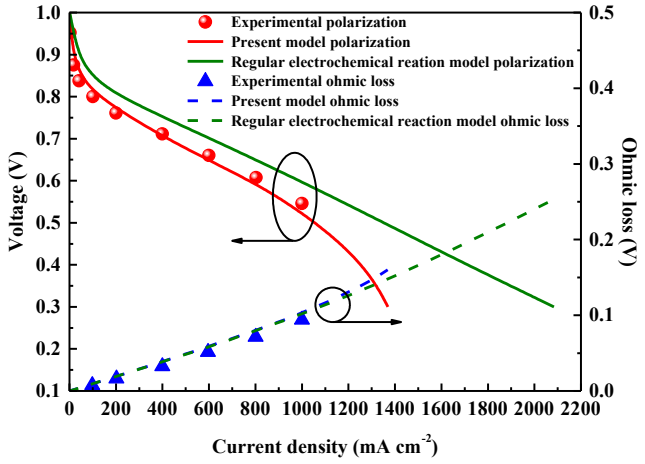

Fig. 2. Model validation.

Table 5
Design parameters of cathode catalyst layer with different Pt loadings.

Case number	Pt loading of CCL (mg cm^{-2})	Thickness of CCL (μm)
1	0.4	40
2	0.3	30
3	0.2	20
4	0.1	10
5	0.05	5

in which y_{bare} is the weight fraction of the bare carbon with zero loading of Pt, and in this study the value of y_{bare} is fixed as 0.

The Pt weight percentage of the Pt/C catalyst $wt\%$ can be obtained by [29]

$$wt\% = \frac{\rho_{Pt}\varepsilon_{Pt}}{\rho_{Pt}\varepsilon_{Pt} + (1 - y_{bare})\rho_C\varepsilon_C} \tag{35}$$

The thickness of ionomer δ_{ion} (m) can be obtained by

$$\delta_{ion} = \left(\left(\frac{\varepsilon_{ion}}{\varepsilon_C} + 1\right)^{1/3} - 1\right) r_C \tag{36}$$

where r_C (m) is the carbon particle radius. The volume fraction of carbon particle ε_C and fraction of ionomer ε_{ion} can be calculated as

$$\varepsilon_C = \frac{1 - \varepsilon_{CCL} - \varepsilon_{Pt}}{1 + \rho_C (I/C)/\rho_{ion}} \tag{37}$$

Table 4
Parameters of electrochemical kinetics.

Parameters	Correlation/value	Unit	Source Refs
Transfer coefficient	$\alpha_a = 0.5$; $\alpha_c = 1.0$		[59]
Volumetric reference exchange current density in anode	$j_{0,a}^{ref} = 4.5 \times 10^7 \exp\left(-1400\left(\frac{1}{T} - \frac{1}{353.15}\right)\right)$	A m^{-3}	[8]
Surface reference exchange current density in cathode	$j_{0,c}^{ref} = 1.0 \exp\left(-\frac{E_c}{R}\left(\frac{1}{T} - \frac{1}{353.15}\right)\right)$	A m^{-2}	[29]
Reference concentration of hydrogen; oxygen	$c_{H_2}^{ref} = 56.4$; $c_{O_2}^{ref} = 3.39$	mol m^{-3}	[62]
Equilibrium potential for Pt oxide formation	$U_{PtO} = 0.76$	V	[33]
Activation energy in oxygen reduction reaction	$E_c = 67000.0$	J mol^{-1}	[29]
Energy parameter for Temkin isotherm	$\omega = 3000.0$	J mol^{-1}	[29]
Interfacial resistance coefficients at the ionomer film surface (k_1), Pt particle surface (k_2)	$k_1 = 8.5$; $k_2 = 25.0$		[29]
Density of carbon particle; ionomer; Pt	$\rho_{C,ion,Pt} = 1800.0$; 2000.0; 21450.0	kg m^{-3}	[29,49]
Pt loading of CCL	$m_{Pt} = 0.1$	mg cm^{-2}	[29,49]
Electrochemical specific area of Pt in cathode	$a_{ECSA} = 70$	m^2_{Pt} g^{-1}_{Pt}	[29]
Ionomer to carbon weight ratio	I/C = 0.75		[49]
Bare carbon mass fraction	$y_{bare} = 0$		[29]
Radius of carbon particle	$r_C = 25$	nm	[29]

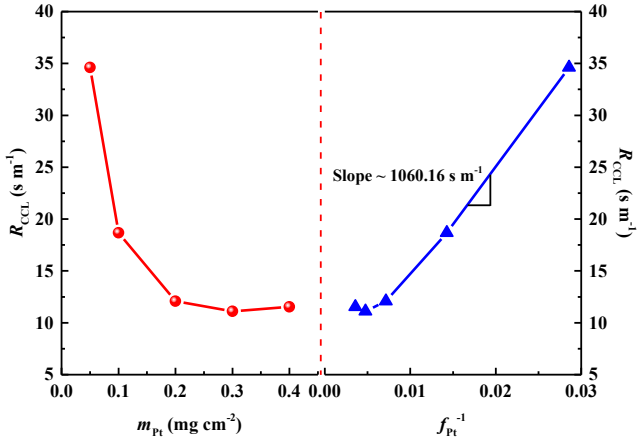

Fig. 3. Effect of Pt loading on the transport resistance of oxygen in CCL.

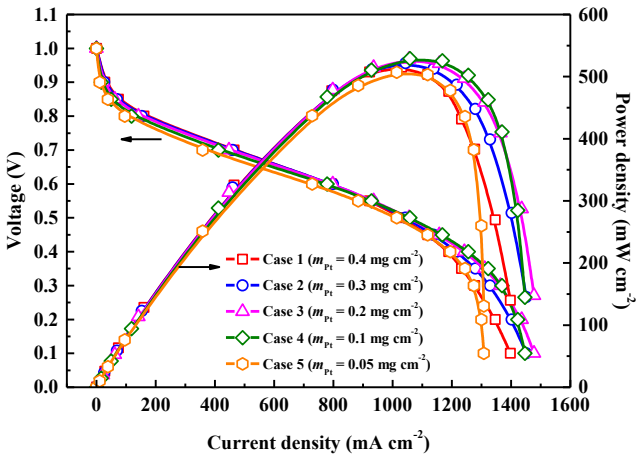

(a) Polarization and power density curves

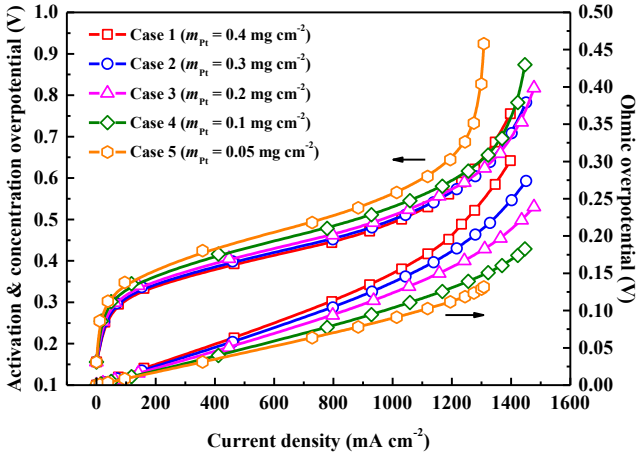

(b) Overpotential

Fig. 4. Effect of Pt loading on performance.

$$\varepsilon_{ion} = 1 - \varepsilon_{CCL} - \varepsilon_{Pt} - \varepsilon_{C} \quad (38)$$

in which the volume fraction of Pt particle can be obtained as

$$\varepsilon_{Pt} = \frac{m_{Pt}}{\delta_{CCL}\rho_{Pt}} \quad (39)$$

All the above parameters can be referred to Table 1 and Table 4.

Come here a discussion on the applicability of some recently proposed sub-models for water saturation-pressure relation and gas

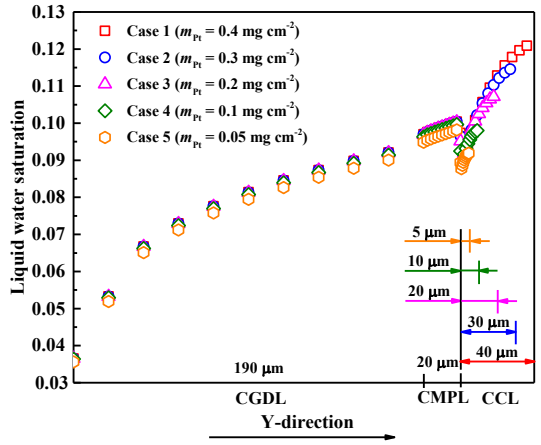

(a) Liquid water saturation distribution in cathode GDL, MPL and CCL (0.6 V)

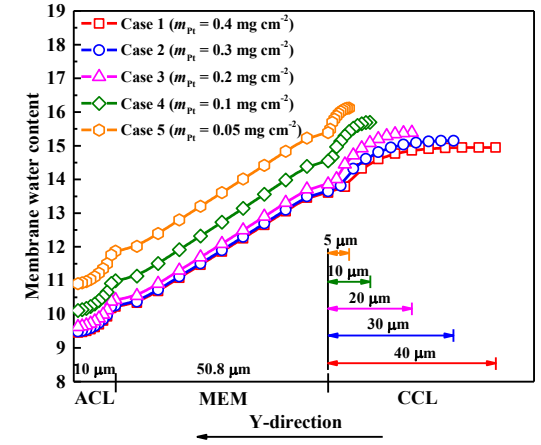

(b) Membrane water content distribution in ACL, MEM and CCL (0.6 V)

Fig. 5. Effect of Pt loading on the water distribution in membrane electrodes.

effective diffusivities is presented. First, it should be noted that the recently developed models for water satruarion-pressure relation [34-37] and for the effective diffusivity [38-44] differ from each other very much and no well-accepted model can be used. For example, at the same water saturation in MPL and CL, the pressure predicted by different models can be different by four-order of magnitude. It is interest to note that in the range of water saturation from zero to about 0.7 the conventional Leverett-J function is a kind of of average of the recently porposed [35] (the minimum) and [37] (the maximum) models in GDL. Second, results comparison have been conducted between one modified model and the above-stated model with Leverett-J function and Bruggeman correction. In the modified model the Leverett-J function is replaced by correlation proposed in [35] and the Bruggemman equation is replaced by equations proposed in [44-48] with all others remain the same. Even though the predicted V-I curve of the modified model differs from the V-I curve of the original model appreciably, the predicted effect of the catalyst parameters, Pt/C ratio and particle diameters, are qualitatively all the same and quantitatively differ not too much. Since the focus of the present paper is to reveal the effect of the five catalyst design parameters, the conventional Leverett-J function and the Bruggemman euqations are still adopted. For the details of comparison see the supplementary material.

2.5. Numerical solution details

The computational domain shown in Fig. 1 is discretized by 150,000 cells, which was determined after a grid-independent examination. The porous layers (GDLs, MPLs and CLs of anode and cathode) and

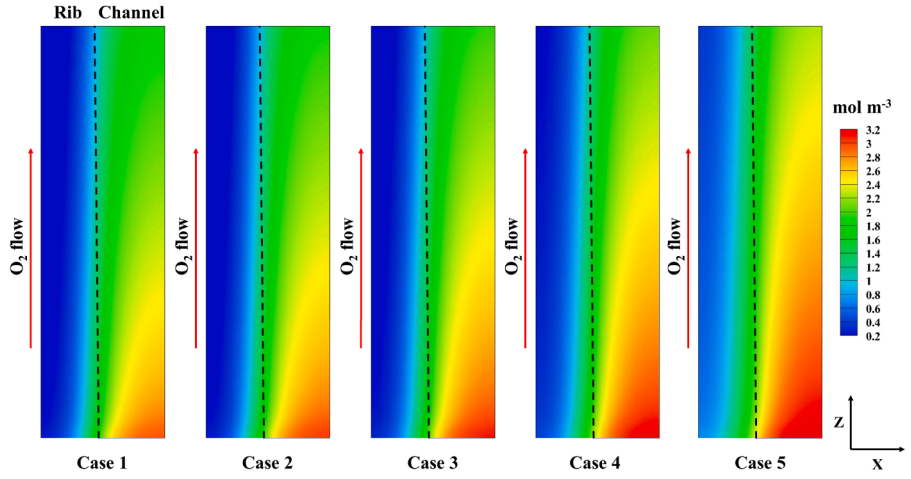

(a) Oxygen concentration in the pore on the middle plane of CCL (0.6 V)

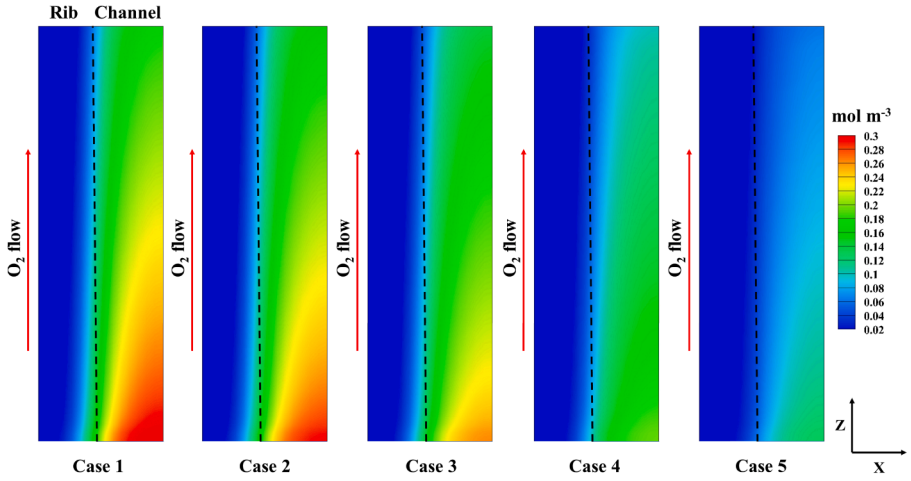

(b) Oxygen concentration on the Pt surface on the middle plane of CCL (0.6 V)

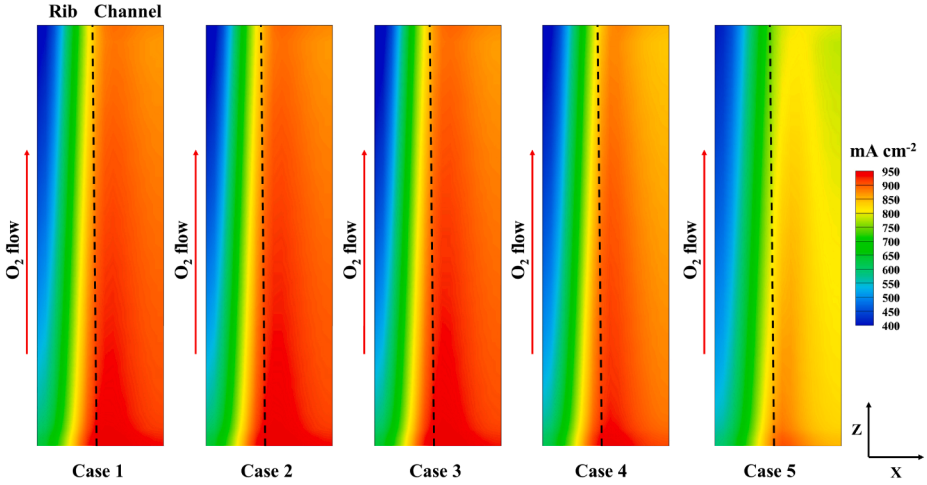

(c) Current density on the middle plane of membrane (0.6 V)

Fig. 6. Effect of Pt loading on the oxygen and current density distribution along the oxygen flow direction.

membrane are all divided into 10 layers along the Y-direction, the size of each mesh in the BP and channel is 1 mm along Z-directions, the mesh sizes in Y-direction for GDL, MPL, CL, MEM are 0.19 mm, 0.02 mm, 0.01 mm, 0.0508 mm, respectively, and on the rest part of other two directions the mesh sizes are all 0.1 mm.

The user-defined functions (UDF) written by C code were

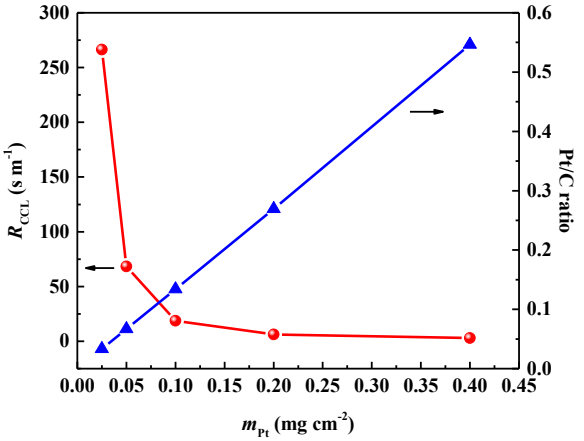

Fig. 7. Effect of Pt/C ratio on the transport resistance.

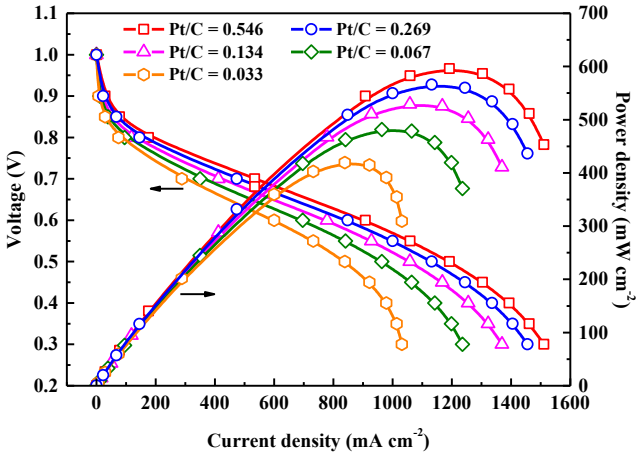

(a) Polarization and power density curves

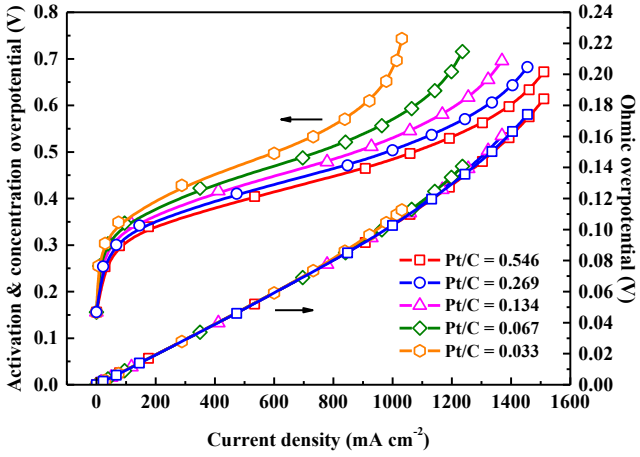

(b) Overpotential

Fig. 8. Effect of Pt/C ratio on performance.

implemented in the computational fluid dynamics (CFD) software Fluent to solve the conservation equations by the means of finite volume method (FVM). In order to ensure the accuracy of the results, a strict convergence criterion of 1.0×10^{-8} for the variable relative change is used for all the 13 governing equations.

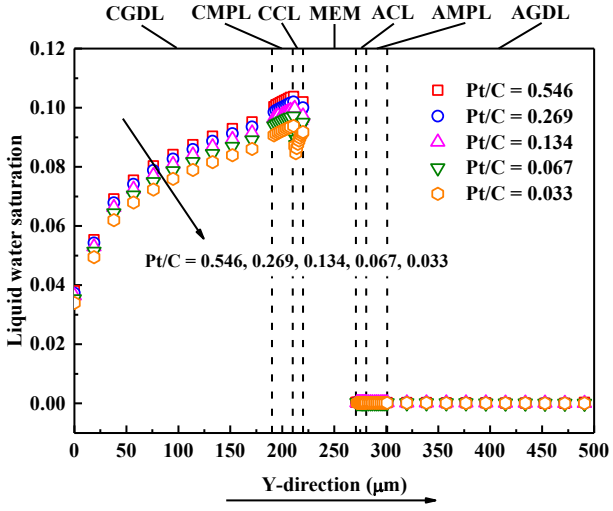

(a) Liquid water saturation distribution (0.6 V)

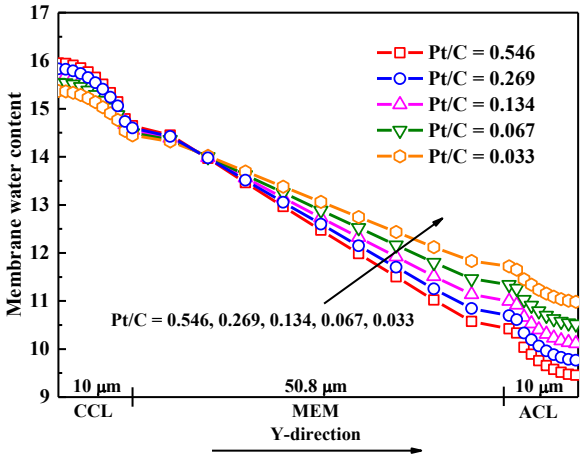

(b) Membrane water content distribution (0.6 V)

Fig. 9. Effect of Pt/C ratio on the water distribution.

3. Results and discussion

The numerical model developed in this study is first applied to the PEMFC provided by [63] for which all the related parameters and operating condition are listed in Table 1.

The simulated polarization curve and ohmic loss are compared with the test data in Fig. 2. As shown in the figure, the predicted results agree well with the test data (V verus I and ohmic loss). In order to compare the regular electrochemical reaction model with the present model, the $c_{O_2}^{Pt}$ in Eq.(26) is replaced by c_{O_2}, which is the oxygen concentration in the pore of CL and does not consider the transport resistance for the oxygen in the composition of electrode paticles, and Eq.(26) is simplified as

$$j_c = k_c (c_{O_2})^{\gamma} \tag{40}$$

In the comparasion simulation, except for the simplifications shown above, all the other details of the regular electrochemical reaction model are all consistent with the present model. It can be found that the polarization curve of the regular model deviates from the experimental data significantly, and in the high current density regions, the regular model dose not reflect the concentration loss, which is physically unacceptable.

In the following, the effects of Pt loading of CCL on the polarization curve, power density curve, voltage loss, water and species

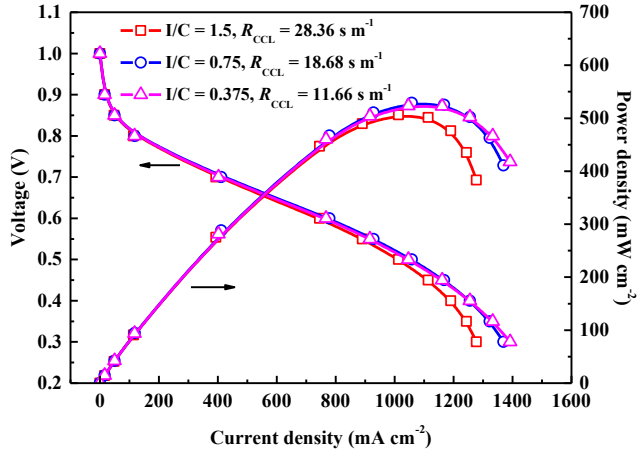

(a) Polarization and power density curves

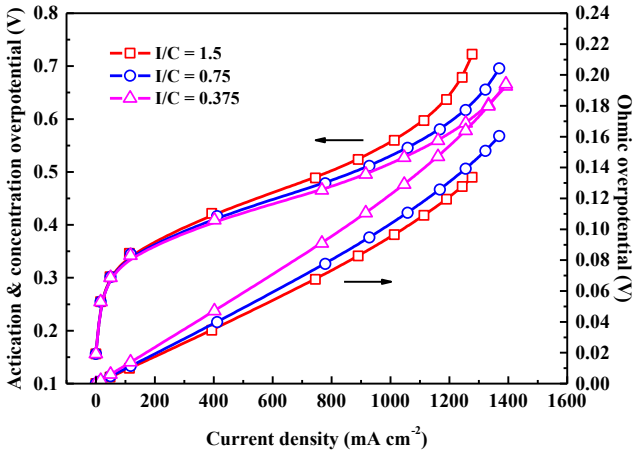

(b) Overpotential

Fig. 10. Effect of I/C ratio on performance.

transportation are discussed firstly in Section 3.1. Then the effects of Pt/C ratio, I/C ratio, carbon particle radius and electrochemical specific area of Pt particles of CCL are evaluated in Sections 3.2, 3.3, 3.4 and 3.5 respectively. It should be noted that the effects of the five factors reflect the improvements in two aspects, the improvement of the cathode model and the comprehensive model of the entire PEMFC. This is because the variation of the cathode model affects the amount of water generation in the cathode, and the variation of generated water further affect its transport in other layers of the fuel cell, which in term affects the transport processes of the entire fuel cell.

3.1. Effect of Pt loading of CCL

Since the cathodic oxidation reaction rate is the key factor limiting the performance of PEMFC, the increase of Pt loading can increase the three-phase reaction area to a certain extent, which can promote the cathodic oxidation reaction rate. In our numerical study, the Pt loading is varied from 0.05 mg cm^{-2} to 0.4 mg cm^{-2}. As shown in Eq. (39), in order to ensure a certain volume fraction of Pt (ε_{Pt}) in CCL, the thickness of the CCL should change correspondingly with the change of the Pt loading. The simulated Pt loadings and the corresponding thicknesses of CCL are listed in Table 5.

The left and right figures of Fig. 3 respetively show the effect of Pt loading (m_{Pt}) and roughness factors on the transport resistance of oxygen in CCL. The transport resistance and roughness factors have following relationship [64]

$$R_{CCL} = \frac{\delta_{CCL}}{3D_{O_2}^{eff}} + \frac{R_{O_2}^{Pt}}{f_{Pt}} \quad (41)$$

where the first term on the right side reflects the contribution of pores to the oxygen transport resistance, $R_{O_2}^{Pt}$ of the second term is the local transport resistance of oxygen ($R_{O_2}^{Pt} = R_{ion,int} + R_{ion}^{eff} + R_{Pt,int}^{eff}$), and f_{Pt} is the roughness factor, which is expressed as,

$$f_{Pt} = 10 a_{ECSA} m_{Pt} \quad (42)$$

From Fig. 3 it can be seen that with the increase of Pt loading, the R_{CCL} decreases sharply at the beginning and then increases very slightly in the range of 0.3 mg cm^{-2} to 0.4 mg cm^{-2}. Such variation pattern depends on the balance between the 1st term and 2nd term of Eq. (41)'s right. As the Pt loading increases, the thickness of CCL increases, however, the second term on the right of Eq. (41) decreases linearly with the increase of m_{Pt}. In the low Pt loading region it plays a leading role causing the rapid decrease of R_{CCL}. But when the Pt loading is large enough (from 0.3 mg cm^{-2} to 0.4 mg cm^{-2}) the effect of the first term on the right side of Eq. (41) beomes significant causing the slight increase of R_{CCL}. Moreover, the values of R_{CCL} shows an aproximate linear relationship with $1/f_{Pt}$ within a wide range of $R_{CCL}$and the slop is about 1060.16 s m^{-1}, which is consistent with the data measured in the range of 100 to 1000 s m^{-1} [65].

Fig. 4(a) shows the polarization and power density curves and Fig. 4(b) shows the corresponding overpotential under five Pt loadings (0.05, 0.1, 0.2, 0.3, 0.4 mg cm^{-2}). As shown in Fig. 4(a), the performance is improved with the increase of Pt loading from 0.05 mg cm^{-2} to 0.2 mg cm^{-2} (from Case 5 to Case 3), but with a further increase of Pt loading, the performance decays obviously. Fig. 4(b) shows the overpotential variation for the five cases. With the increase of Pt loading, the activation and concentration overpotential are reduced, which is consistent with the effect of Pt loading on the R_{CCL} (Fig. 3), but due to the increase of the corresponding thickness of the CCL, the ohmic overpotential increases appreciably. Therefore, there exists the best Pt loading, which is the result of the balance between the ohmic overpotential and activation and concentration overpotential, and for the cases studied the amount of 0.2 mg cm^{-2} is preferred.

Fig. 5 shows the effect of Pt loading on the water distribution in the membrane electrode. As shown in Fig. 5(a), with the increase of Pt loading, the liquid water saturation in cathode increases, especially in CCL. This is mainly caused by the fact that with the increase of Pt loading, more water is generated due to the improvement of performance; in addition, the increase of water transport resistance due to the increase of CCL thickness could also be a reason. Moreover, due to different contact angels, permeabilities and porosities of the CL, MPL, and GDL, there exist liquid saturation jumps at the interfaces of CCL/CMPL and CMPL/CGDL. Fig. 5(b) shows the membrane water content distribution in membrane electrodes under five Pt loadings. With the decrease of Pt loading, the membrane water content in membrane electrodes increases. This variation trend can be explained as follows. When the thickness of CCL is thinner, the transmembrane penetration of water due to the liquid pressure imbalance between anode and cathode becomes easier, as shown in the source term of membrane water content in Table 2, and this makes the membrane water content of anode increase and then makes the membrane water content in the whole membrane electrodes increase because of the diffusion effects.

The effect of Pt loading on the oxygen transport process and current density distribution is shown in Fig. 6 where the oxygen and current density distributions on the middle plane of CCL along the oxygen flow direction under five Pt loading cases are presented. As shown in Fig. 6(a), with the decrease of Pt loading from Case 1 to Case 5, the transport resistance of oxygen in the pore of CCL decreases due to the decrease of CCL thickness, which leads to the increase of oxygen concentration in the pore of CCL. However, due to the decrease of CCL thickness, the reaction rate per unit volume increases, and the oxygen consumption increases, which leads to the decrease of oxygen

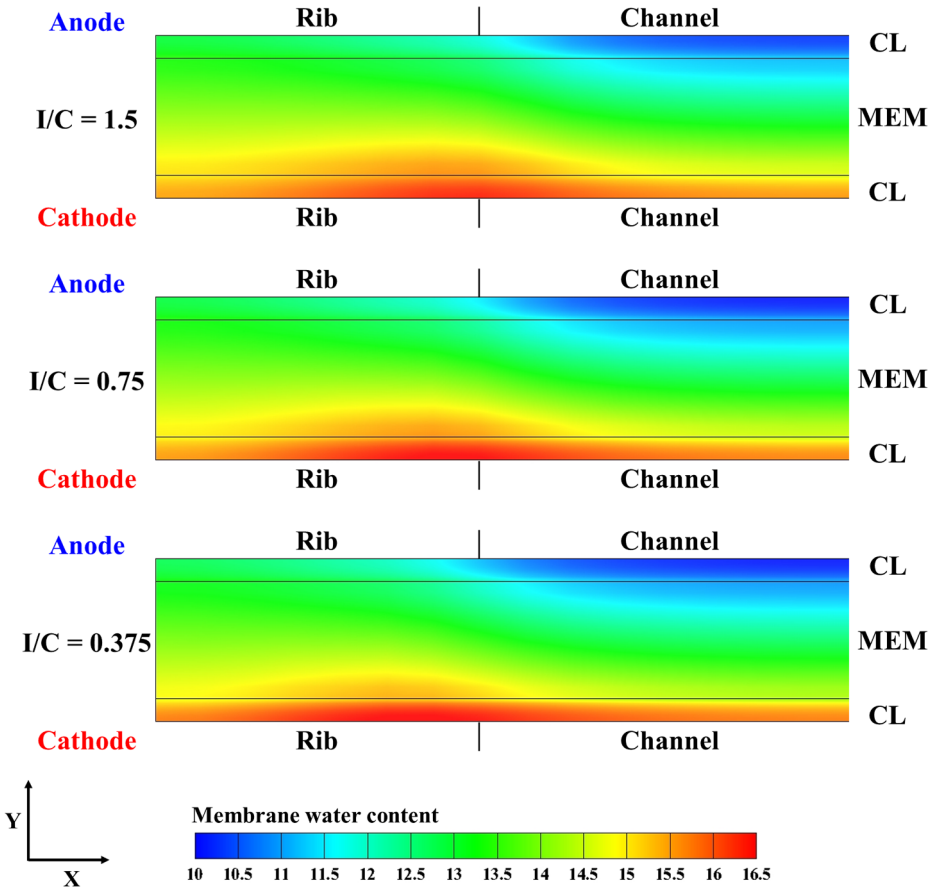

Fig. 11. Effect of I/C ratio on the membrane water distribution on the center section (0.6 V).

concentration on Pt surface from Case 1 to Case 5 (Fig. 6(b)). This may suggest that a low Pt loading is more likely to cause oxygen starvation. For the current density distribution (Fig. 6(c)), with the decrease of Pt loading from Case 1 to Case 5, the current density decreases especially for Case 4 and Case 5. Moreover, the maximum current density appears under the flow channel because the oxygen concentration in the CCL under the channel is the highest. It should be noted that even the anode and cathode stoichiometry is 3.0, the current density distribution on the middle plane of membrane along the oxygen flow direction is not uniform, and the current density near the inlet of cathode is much higher than the outlet. Therefore, the process still obviously shows three-dimensional multiphase non-isothermal flow characteristics.

3.2. Effect of Pt/C ratio of CCL

In order to evaluate the effect of Pt/C ratio, the thickness of CCL is fixed as 10 μm and the Pt loading changes from 0.025 mg cm^{-2} to 0.4 mg cm^{-2}. Fig. 7 shows the relationships between Pt loading versus R_{CCL} and Pt/C ratio. With the increase of Pt loading, the R_{CCL} decreases sharply at the beginning, and then gradually flattens, while the Pt/C ratio increases linearly. In the following the effect of Pt/C ratio is presented.

Fig. 8 shows the effect of Pt/C ratio on the performance. The polarization and power density curves with five Pt loadings (Pt/C ratios) are shown in Fig. 8(a). It can be seen that the increase of Pt loading (Pt/C ratio) from 0.025 mg cm^{-2} to 0.05 mg cm^{-2} can enhance the performance significantly, but with a further increase of Pt loading (Pt/C ratio), the improvement is gradually weakened. Corresponding to the polarization (Fig. 8(a)), Fig. 8(b) shows the overpotential. Due to the increase of Pt loading (Pt/C ratio), the activation and concentration overpotentials decrease significantly, but the change on the ohmic overpotential is negligible which is different from Fig. 4(b) where CCL thickness increases with Pt loading.

The Pt/C ratio also has a significant effect on the corresponding water distribution. Fig. 9(a) shows that the liquid water saturation in cathode increases significantly with the increase of Pt/C ratio (Pt loading), which is mainly due to the improvement of performance with the increase of Pt loading, however, the variation of liquid water saturation in anode can not be observed. Moreover, Pt/C ratio also has a significant effect on the membrane water content distribution in the membrane electrode as shown in Fig. 9(b). The membrane water content of ACL decreases with the increase of Pt loading (Pt/C ratio), but the membrane water content in CCL has the opposite variation trend.This is mainly caused by the effect of electro-osmotic drag (EOD).

3.3. Effect of I/C ratio of CCL

For the manufacture of the CL, the I/C ratio is a very important parameter, which is defined as

$$\text{I/C ratio} = \frac{m_{ion}}{m_C} \tag{43}$$

where m_{ion} (mg cm^{-2}) and m_C (mg cm^{-2}) are the weight per unit area of Nafion and carbon respectively. The increase of Nafion content in CL produces more path for the transfer of proton and membrane water, meanwhile when the Nafion layer thickness increases, the oxygen diffusion may be weakened [66] and the effective reaction area may be reduced. Thus, a proper I/C ratio is very important for the improvement of proton conductivity, electron conductivity, membrane water diffusivity and oxygen diffusivity. Three I/C ratios of CCL (1.5, 0.75 and 0.375) are numerically simulated on its effect on the fuel cell performance, on the distributions of oxygen transport resistance, and on

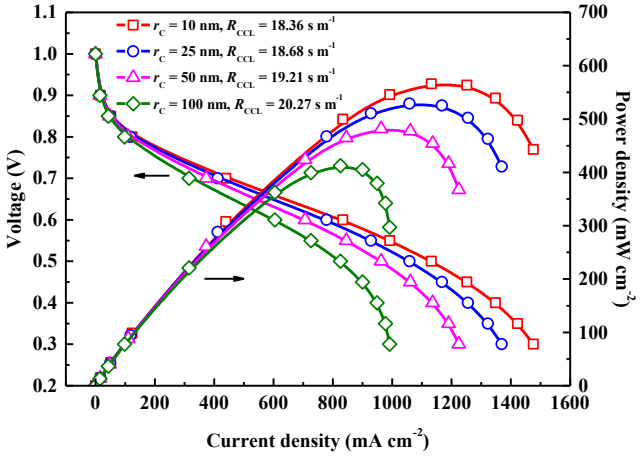

(a) Polarization and power density curves

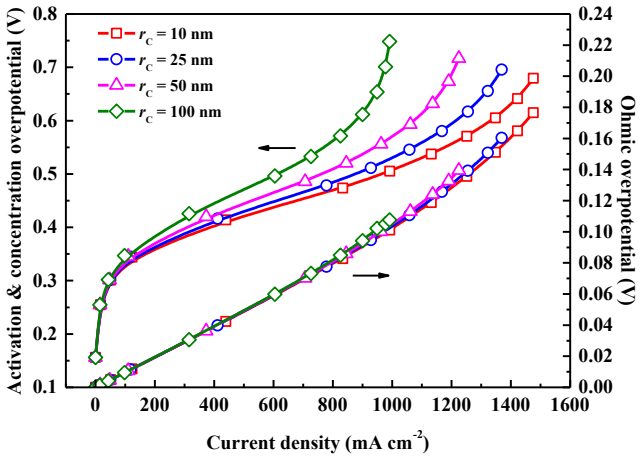

(b) Overpotential

Fig. 12. Effect of carbon particle radius on performance.

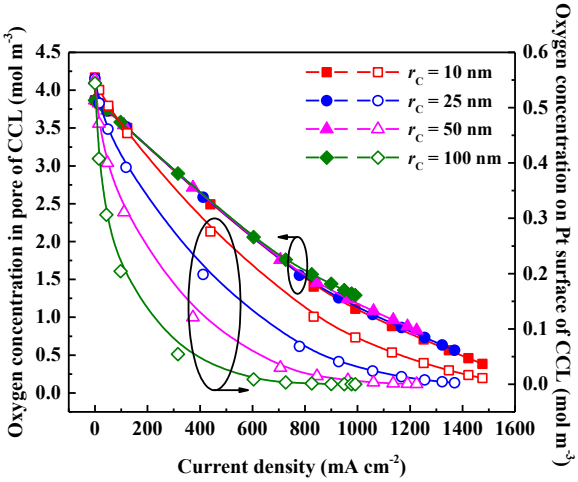

Fig. 13. Effect of carbon particle radius on the oxygen concentration.

membrane water distribution in membrane electrode.

Fig. 10 shows the effect of I/C ratio on the performance, including the polarization and power density curve (Fig. 10(a)) and the overpotential (Fig. 10(b)). As shown in Fig. 10(a), both the polarization curves and the power density curves for I/C ratio of 0.375 and 0.75 are very close to each other, but when the I/C ratio is 1.5, both the voltage and power density have an appreciable decrease in the high current density region because of the increased oxygen transport resistance. For the effect on the overpotential Fig. 10(b) shows that with the increase of I/C ratio, the activation overpotential increases while the ohmic overpotential decreases..

Fig. 11 shows the effect of I/C ratio on the membrane water distribution in the center section perpendicular to the flow direction. Comparing the three cases, with the increase of I/C ratio, some improvement can be found in the uniformity of the membrane water distribution. This is because membrane water diffusivity increases with the increase of I/C ratio. It is suggested that the increase in I/C ratio is better for the uniformity of membrane water distribution.

3.4. Effect of carbon particle radius of CCL

In the structure of CL the carbon particles serve as the carriers of Pt particles, and the carbon particle size is closely related to the effective reaction area. The decrease of carbon particle size contributes to the reduction of the activation loss for fixed carbon content. Simulations are conducted for the carbon particle radius ranging from 10 nm to 100 nm to evaluate its effect on the performance and oxygen transport process in CCL.

As shown in Fig. 12(a), the polarization and power density curves are enhanced appreciably by the decrease of carbon particle radius. This enhancement is mainly due to the reduction of activation and concentration overpotential as shown in Fig. 12(b), meanwhile the decrease of carbon particle radius can reduce the oxygen transport resistance (R_{CCL}). As shown in Fig. 12(b), the carbon particle radius has little effect on the ohmic overpotential .

Fig. 13 shows the effect of carbon particle radius on the oxygen concentration in the pore of CCL and on the oxygen concentration on the Pt surface of CCL. With the decrease of carbon particle radius, the oxygen concentration on the Pt surface increases significantly, which is important to reduce the concentration loss and mitigate the oxygen starvation under high current density. However, the change of carbon particle radius has little effect on the oxygen transport resistance in the pore of CCL.

Fig. 14 shows the effect of carbon particle radius on the oxygen concentration on the Pt surface distribution in CCL center section along the flow direction. It can be found that the oxygen concentration on the Pt surface under the channel is higher than that under the rib, and the oxygen concentration on the Pt surface decreases from the CGDL side to the MEM side, which is due to its consumption of electrochemical reaction and the transport resistance of oxygen. Moreover, with the increase of carbon particle radius, the oxygen concentration on the Pt surface decreases significantly, and when the carbon particle radius is 100 nm, the oxygen concentration on the Pt surface is very low.

3.5. Effect of the ECSA of Pt particles of CCL

The ECSA of Pt particles is directly related to the effective reaction area of CL. Three cases with different ECSA of Pt particles ranging from 50 to 100 $m^2_{Pt}\ g^{-1}_{Pt}$ are investigated to study its effect on the performance and oxygen transport resistance in CCL.

Fig. 15 shows the effect of ECSA of Pt particles on the performance. As shown in Fig. 15(a), the output performance is improved by the increase of ECSA, and the improvement is appreciable for the limiting current density. Fig. 15(b) shows the effect of ECSA on the overpotential, and it can be found that the effect of ECSA on the activation and concentration overpotential is detectable in the high current density (larger than 1000 mA cm^{-2}), however, its effect on the ohmic overpotential is little.

4. Conclusions

In this study, a macroscopic three-dimensional multiphase non-

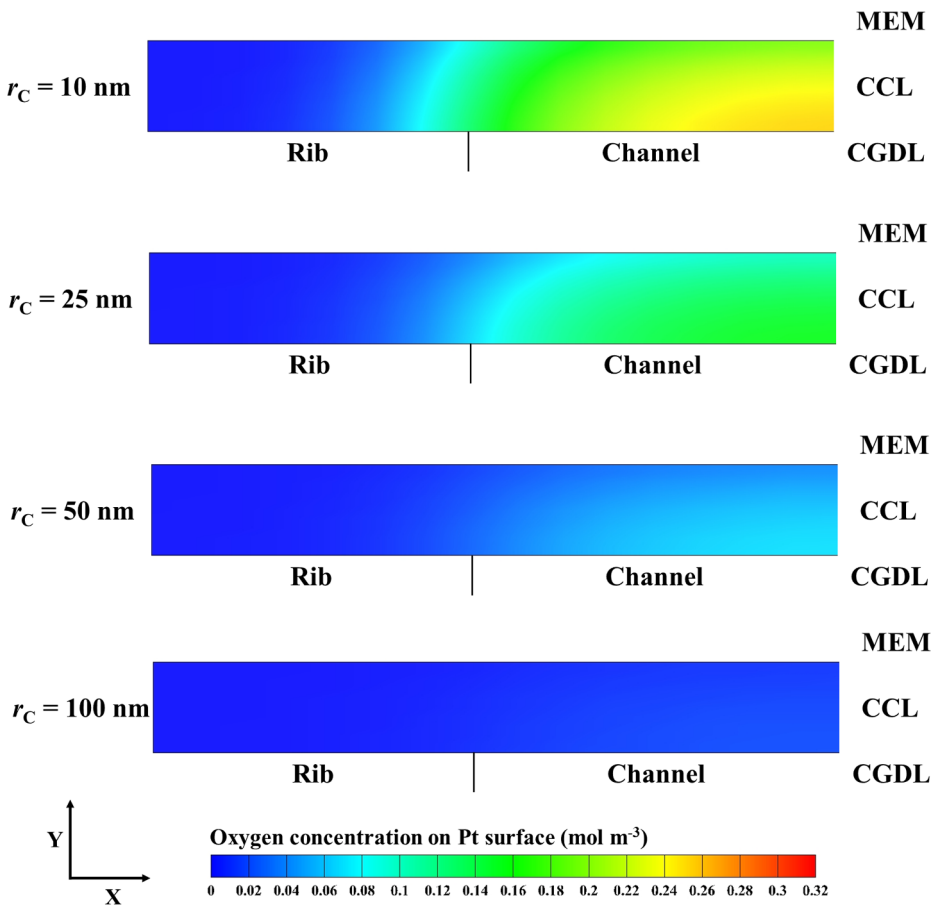

Fig. 14. Effect of carbon particle radius on the oxygen concentration on the Pt surface distribution in CCL center section perpendicular to the flow direction (0.6 V).

isothermal polymer electrolyte membrane fuel cell (PEMFC) model coupled with an improved electrochemical kinetics model considering the geometric structure parameters of the cathode catalyst layer (CCL) and oxygen transport process in CCL is developed. The effects of five CCL design parameters are investigated. Based on the conditions and the model used in the present study, following conclusions can be derived:

1. The Pt loading of CCL has a significant effect on the performance. For the PEMFC studied, there exists the best Pt loading of CCL (around 0.2 mg cm^{-2}).
2. With the decrease of Pt loading, the oxygen concentration in the pore of CCL increases, but the oxygen concentration on the Pt surface of CCL decreases, and a low Pt loading is more likely to cause oxygen starvation.
3. The increase of Pt/C ratio can promote the performance significantly at a lower Pt/C ratio, and with its further increase, the improvement gradually weakened.
4. The activation and concentration overpotentials decrease significantly with the increase of Pt/C ratio, but the change of the ohmic overpotential is not obvious.
5. A lower I/C ratio (say, I/C = 0.375) is good for the enhancement of limiting current density, and a larger I/C ratio (say, I/C = 0.75) is good for the increase of maximum power density. But a too-large I/C ratio has negative effect on improving the limiting current density and maximum power density.
6. The increase in I/C ratio is better for the uniformity of membrane water distribution.
7. With the decrease of carbon particle radius, the oxygen concentration on the Pt surface of CCL increases significantly, while the effect of carbon particle radius on the oxygen concentration in the pore of CCL is very weak.
8. With the increase of ECSA of Pt particles, the performance is promoted, and this promotion is caused by the reduction of activation and concentration overpotential, especially the concentration overpotential.

It is to be noted that the validatidy of the above conlcusions need to be further verified within a wider parameter range, and this is underway in the authors' group with adopting more recent submodels.

CRediT authorship contribution statement

Pu He: Conceptualization, Methodology, Software, Validation, Formal analysis, Writing - original draft. **Yu-Tong Mu:** Methodology, Funding acquisition. **Jae Wan Park:** Resources. **Wen-Quan Tao:** Resources, Writing - review & editing, Visualization, Supervision, Project administration, Funding acquisition.

Declaration of Competing Interest

The authors declare that they have no known competing financial interests or personal relationships that could have appeared to influence the work reported in this paper.

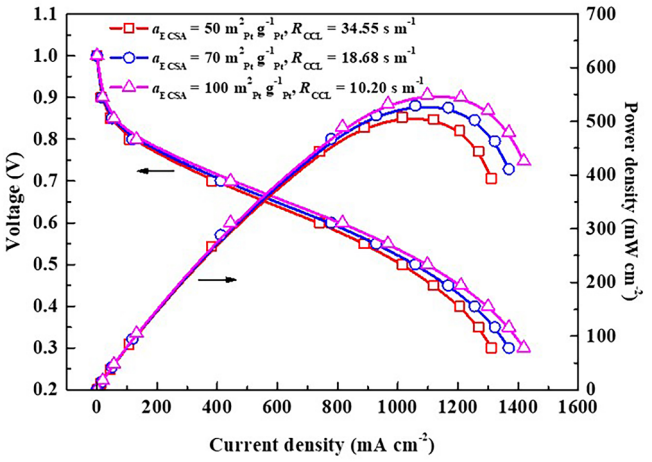

(a) Polarization and power density curves

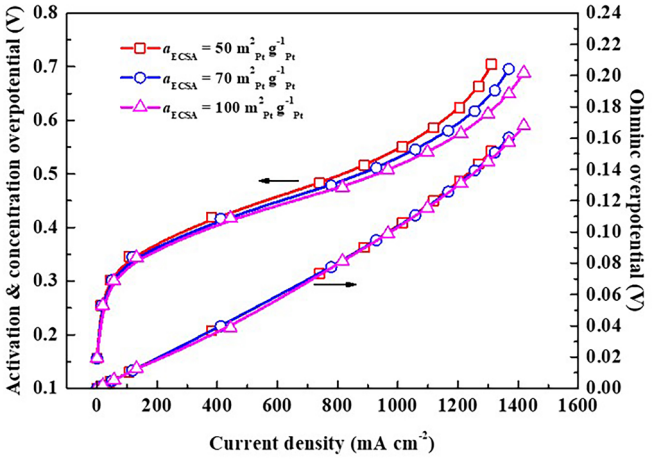

(b) Overpotential

Fig. 15. Effect of ECSA of Pt particles on performance.

Acknowledgments

This research is supported by the Key Project of the National Natural Science Foundation of China (Grant No. 51836005), the National key research and development project of China (Grant No. 2017YFB0102702), the National Natural Science Foundation of China (51806170), the Key Science and Technology Project in Henan Province (Innovation Leading Project: 191110210200) , the Basic Research Project of Shaanxi Province (2019) and the 111 Project (B16038).

Appendix A. Supplementary data

Supplementary data to this article can be found online at https://doi.org/10.1016/j.apenergy.2020.115555.

References

[1] DOE hydrogen and fuel cells program review: fuel cell vehicle and bus cost analysis. Department of Energy; 2015.
[2] Wu HW. A review of recent development: Transport and performance modeling of PEM fuel cells. Appl Energy 2016;165:81–106.
[3] Nguyen TV. A Water and Heat Management Model for Proton-Exchange-Membrane Fuel Cells. J Electrochem Soc 1993;140:2178–86.
[4] Fuller TF. Water and Thermal Management in Solid-Polymer-Electrolyte Fuel Cells. J Electrochem Soc 1993;140:1218–25.
[5] Berning T, Djilali N. Three-dimensional computational analysis of transport phenomena in a PEM fuel cell - a parametric study. J Power Sources 2003;124:440–52.
[6] Lum KW, McGuirk JJ. Three-dimensional model of a complete polymer electrolyte membrane fuel cell - model formulation, validation and parametric studies. J Power Sources 2005;143:103–24.
[7] Liu X, Tao W, Li Z, He Y. Three-dimensional transport model of PEM fuel cell with straight flow channels. J Power Sources 2006;158(1):25–35.
[8] Jiao K, Li X. Three-dimensional multiphase modeling of cold start processes in polymer electrolyte membrane fuel cells. Electrochim Acta 2009;54:6876–91.
[9] Jiao K, He P, Du Q, Yin Y. Three-dimensional multiphase modeling of alkaline anion exchange membrane fuel cell. Int J Hydrogen Energy 2014;39:5981–95.
[10] Mu YT, Weber AZ, Gu ZL, Schuler T, Tao WQ. Mesoscopic analyses of the impact of morphology and operating conditions on the transport resistances in a proton-exchange-membrane fuelcell catalyst layer. Sustain Energy Fuels 2020;4:3623–39.
[11] Shah AA, Kim GS, Gervais W, Young A, Promislow K, Li J, et al. The effects of water and microstructure on the performance of polymer electrolyte fuel cells. J Power Sources 2006;160:1251–68.
[12] Secanell M, Karan K, Suleman A, Djilali N. Multi-variable optimization of PEMFC cathodes using an agglomerate model. Electrochim Acta 2007;52:6318–37.
[13] Jain P, Biegler LT, Jhon MS. Sensitivity of PEFC models to cathode layer microstructure. J Electrochem Soc 2010;157(8):B1222–9.
[14] Moore M, Wardlaw P, Dobson P, Boisvert JJ, Putz A, Spiteri RJ, et al. Understanding the effect of kinetic and mass transport processes in cathode agglomerates. J Electrochem Soc 2014;161:E3125–37.
[15] Wang Q, Eikerling M, Song D, Liu Z. Structure and performance of different types of agglomerates in cathode catalyst layers of PEM fuel cells. J Electroanal Chem 2004;573:61–9.
[16] Xia Z, Wang Q, Eikerlitig M, Liu Z. Efffectiweness factor of Pt utilization in cathode catalyst layer of polymer electrolyte fuel cells. Can J Chem 2008;86:657–67.
[17] Chan SH, Tun WA. Catalyst layer models for proton exchange membrane fuel cells. Chem Eng Technol 2001;24(1):51–7.
[18] Song D, Wang Q, Liu Z, Navessin T, Holdcroft S. Numerical study of PEM fuel cell cathode with non-uniform catalyst layer. Electrochim Acta 2004;50(2–3):731–7.
[19] Obut S, Alper E. Numerical assessment of dependence of polymer electrolyte membrane fuel cell performance on cathode catalyst layer parameters. J Power Sources 2011;196(4):1920–31.
[20] Marquis J, Coppens MO. Achieving ultra-high platinum utilization via optimization of PEM fuel cell cathode catalyst layer microstructure. Chem Eng Sci 2013;102:151–62.
[21] Suzuki T, Kudo K, Morimoto Y. Model for investigation of oxygen transport limitation in a polymer electrolyte fuel cell. J Power Sources 2013;222:379–89.
[22] Holdcroft S. Fuel cell catalyst layers: A polymer science perspective. Chem Mater 2014;26(1):381–93.
[23] Epting WK, Gelb J, Litster S. Resolving the three-dimensional microstructure of polymer electrolyte fuel cell electrodes using nanometer-scale X-ray computed tomography. Adv Funct Mater 2012;22(3):555–60.
[24] Epting WK, Litster S. Effects of an agglomerate size distribution on the PEFC agglomerate model. Int J Hydrogen Energy 2012;37(10):8505–11.
[25] Greszler TA, Caulk D, Sinha P. The impact of platinum loading on oxygen transport resistance. J Electrochem Soc 2012;159:F831–40.
[26] Owejan JP, Owejan JE, Gu W. Impact of Platinum Loading and Catalyst Layer Structure on PEMFC Performance. J Electrochem Soc 2013;160:F824–33.
[27] Kudo K, Morimoto Y. Analysis of Oxygen Transport Resistance of Nafion thin film on Pt electrode. ECS Trans 2012;53(2):1487–94.
[28] Kudo K, Suzuki T, Morimoto Y. Analysis of oxygen dissolution rate from gas phase into Nafion surface and development of an agglomerate model. ECS Trans 2010;33(1):1495–502.
[29] Hao L, Moriyama K, Gu W, Wang CY. Modeling and experimental validation of Pt loading and electrode composition effects in PEM fuel cells. J Electrochem Soc 2015;162(8):F854–67.
[30] Jiao K, Li X. Water transport in polymer electrolyte membrane fuel cells. Prog Energy Combust Sci 2011;37:221–91.
[31] Zhang G, Fan L, Sun J, Jiao K. A 3D model of PEMFC considering detailed multiphase flow and anisotropic transport properties. Int J Heat Mass Transf 2017;115:714–24.
[32] Subramanian NP, Greszler T, Zhang J, Gu W, Makharia RR. Pt-Oxide Coverage-Dependent Oxygen Reduction Reaction (ORR) Kinetics. ECS Trans 2011;41:985–1008.
[33] Yoon W, Weber AZ. Modeling Low-Platinum-Loading Effects in Fuel-Cell Catalyst Layers. J Electrochem Soc 2011;158(8):B1007–18.
[34] Ye Q, Nguyen TV. Three-Dimensional Simulation of Liquid Water Distribution in a PEMFC with Experimentally Measured Capillary Functions. J Electrochem Soc 2007;154(12):B1242–51.
[35] Gostick JT, Ioannidis MA, Fowler MW, Pritzker MD. Direct measurement of the capillary pressure characteristics of water–air–gas diffusion layer systems for PEM fuel cells. Electrochem Commun 2008;10:1520–3.
[36] Nguyen TV, Lin G, Ohn H, Wang X. Measurement of capillary pressure property of gas diffusion media used in proton exchange membrane fuel cells. Electrochem Solid-State Lett 2008:11.
[37] Lamanna JM, Bothe JV, Zhang FY, Mench MM. Measurement of capillary pressure in fuel cell diffusion media, micro-porous layers, catalyst layers, and interfaces. J Power Sources 2014;271:180–6.
[38] Martínez MJ, Shimpalee S, Van Zee JW. Measurement of MacMullin Numbers for PEMFC Gas-Diffusion Media. J Electrochem Soc 2009;156:B80.
[39] Wang S, Wang Y. Investigation of the through-plane effective oxygen diffusivity in the porous media of PEM fuel cells: Effects of the pore size distribution and water saturation distribution. Int J Heat Mass Transf 2016;98:541–9.
[40] Zamel N, Astrath NGC, Li X, Shen J, Zhou J, Astrath FBG, et al. Experimental measurements of effective diffusion coefficient of oxygen-nitrogen mixture in PEM

fuel cell diffusion media. Chem Eng Sci 2010;65:931–7.
[41] Nam JH, Kaviany M. Effective diffusivity and water-saturation distribution in single- and two-layer PEMFC diffusion medium. Int J Heat Mass Transf 2003;46:4595–611.
[42] Mezedur MM, Kaviany M, Moore W. Effect of pore structure, randomness and size on effective mass diffusivity. AIChE J 2002;48:15–24.
[43] Tomadakis MM, Sotirchos SV. Ordinary, transition, and Knudsen regime diffusion in random capillary structures. Chem Eng Sci 1993;48:3323–33.
[44] Hwang GS, Weber AZ. Effective-Diffusivity Measurement of Partially-Saturated Fuel-Cell Gas-Diffusion Layers. J Electrochem Soc 2012;159:F683–92.
[45] Chan C, Zamel N, Li X, Shen J. Experimental measurement of effective diffusion coefficient of gas diffusion layer/microporous layer in PEM fuel cells. Electrochim Acta 2012;65:13–21.
[46] Andisheh-Tadbir M, El Hannach M, Kjeang E, Bahrami M. An analytical relationship for calculating the effective diffusivity of micro-porous layers. Int J Hydrogen Energy 2015;40:10242–50.
[47] Inoue G, Yokoyama K, Ooyama J, Terao T, Tokunaga T, Kubo N, et al. Theoretical examination of effective oxygen diffusion coefficient and electrical conductivity of polymer electrolyte fuel cell porous components. J Power Sources 2016;327:610–21.
[48] Sabharwal M, Pant LM, Patel N, Secanell M. Computational Analysis of Gas Transport in Fuel Cell Catalyst Layer under Dry and Partially Saturated Conditions. J Electrochem Soc 2019;166:F3065–80.
[49] Xie B, Zhang G, Xuan J, Jiao K. Three-dimensional multi-phase model of PEM fuel cell coupled with improved agglomerate sub-model of catalyst layer. Energy Convers Manag 2019;199:112051.
[50] Ahmed DH, Sung HJ, Bae J, Lee DR. Reactants flow behavior and water management for different current densities in PEMFC. Int J Heat Mass Transf 2008;51(7–8):2006–19.
[51] Meng H. Numerical studies of liquid water behaviors in PEM fuel cell cathode considering transport across different porous layers. Int J Hydrogen Energy 2010;35(11):5569–79.
[52] Sahraoui M, Bichioui Y, Halouani K. Three-dimensional modeling of water transport in PEMFC. Int J Hydrogen Energy 2013;38(20):8524–31.
[53] Sun J, Guo T, Deng H, Jiao K, Huang X. Effect of electrode variable contact angle on the performance and transport characteristics of passive direct methanol fuel cells. Int J Hydrogen Energy 2015;40(33):10568–87.
[54] Hou Y, Zhang G, Qin Y, Du Q, Jiao K. Numerical simulation of gas liquid two-phase flow in anode channel of low-temperature fuel cells. Int J Hydrogen Energy 2017;42(5):3250–8.
[55] Nonoyama N, Okazaki S, Weber AZ, Ikogi Y, Yoshida T. Analysis of Oxygen-Transport Diffusion Resistance in Proton-Exchange-Membrane Fuel Cells. J Electrochem Soc 2011;158(4):B416–23.
[56] Lange KJ, Sui PC, Djilali N. Pore Scale Simulation of Transport and Electrochemical Reactions in Reconstructed PEMFC Catalyst Layers. J Electrochem 2010;157(10):B1434–42.
[57] Park J, Oh H, Lee YI, Min K, Lee E, Jyoung J. Effect of the pore size variation in the substrate of the gas diffusion layer on water management and fuel cell performance. Appl Energy 2016;171:200–12.
[58] Park S, Popov N. Effect of a GDL based on carbon paper or carbon cloth on PEM fuel cell performance. Fuel 2011;90:436–40.
[59] Fan L, Zhang G, Jiao K. Characteristics of PEMFC operating at high current density with low external humidification. Energy Convers Manag 2017;150:763–74.
[60] Springer TE, Zawodzinski TA, Gottesfeld S. Polymer Electrolyte Fuel Cell Model. J Electrochem Soc 1991;138:2334–42.
[61] Motupally S, Becker AJ, Weidner JW. Diffusion of Water in Nafion 115 Membranes. J Electrochem Soc 2000;147(9):3171–7.
[62] Cao TF, Lin H, Chen L, He YL, Tao WQ. Numerical investigation of the coupled water and thermal management in PEM fuel cell. Appl Energy 2013;112:1115–25.
[63] Ozen DN, Timurkutluk B, Altinisik K. Effects of operation temperature and reactant gas humidity levels on performance of PEM fuel cells. Renew Sustain Energy Rev 2016;59:1298–306.
[64] Schuler T, Chowdhury A, Freiberg AT, Sneed B, Spingler FB, Tucker MC, et al. Fuel-Cell Catalyst-Layer Resistance via Hydrogen Limiting-Current Measurements. J Electrochem Soc 2019;166(7):F3020–31.
[65] Mu YT, Weber AZ, Gu ZL, Tao WQ. Mesoscopic modeling of transport resistances in a polymer-electrolyte fuel-cell catalyst layer: Analysis of hydrogen limiting currents. Appl Energy 2019;255:113895.
[66] Lopez-Haro M, Guétaz L, Printemps T, Morin A, Escribano S, Jouneau PH, et al. Three-dimensional analysis of Nafion layers in fuel cell electrodes. Nat Commun 2014;5:5229.